DEVELOPMENT OF A COUPLED ORBIT-ATTITUDE PROPAGATOR FOR SPACECRAFT OF ARBITRARY GEOMETRY

A Thesis

Submitted to the Faculty

of

Purdue University

by

Sebastian Tamrazian

In Partial Fulfillment of the

Requirements for the Degree

of

Master of Science in Aeronautics and Astronautics

May 2019

Purdue University

West Lafayette, Indiana

THE PURDUE UNIVERSITY GRADUATE SCHOOL
STATEMENT OF THESIS APPROVAL

Professor David A. Spencer

School of Aeronautics and Astronautics

Professor Alina A. Alexeenko

School of Aeronautics and Astronautics

Professor Steven H. Collicott

School of Aeronautics and Astronautics

Approved by:

Professor Weinong Wayne Chen

Aeronautics and Astronautics Associate Head for Graduate Education

To my parents

ACKNOWLEDGMENTS

I want to first thank the friends I've made here at Purdue that I've had the pleasure of going through the ups and downs of university life with. I never would have guessed six years ago that moving from the west coast to the middle of Indiana would end up being one of the best choices I've made, but I've met some of my best friends here on campus, and I couldn't have gotten through this without them. Thank you to Matt, Pins, Korba, Josh, and Mike for making my time at home with you guys so enjoyable, and thank you to Omar and Yash for the great company in the lab on those 3AM type of assignments. Thank you to Matt, Mac, and Aaron for sticking it out with me here and for those great SASSI2 moments, and to the whole aero crew of '17 for the fond memories.

I especially want to thank my whole research group at the Space Flight Projects Lab (SFPL) for all of their help and enthusiasm. I'm incredibly grateful to be a member of a community with such intellectual curiosity, and so eager to give help and advice. I want to especially thank Jay for all the guidance in setting up the propagators, Mac and Rohan for some great conversation and helpful career advice, and Sylvain for helping me with mission implementation work for my FEMTA tasks.

Further, I want to thank Dr. Anthony 'Tony' Cofer, Arly, Sammy, Ben, Brandon, and Mayank for all the great work on ADE over the years, and all of the 60+ students who have contributed to the project over the years at Purdue. Thank you also to Liam, Dr. John Bellardo, and the rest of the Cal Poly team for all the great work. Working on ADE with all of you has been such a valuable experience, and I'm so grateful to have had this opportunity.

There have been many people outside of the SFPL who have also helped me with this project. A big thank you to Dr. Alexandra Long for laying out so much of the groundwork for what's written here, and to Dr. Israel Sebastião for invaluable help

with the DSMC setup. Thank you also to Alberto Cebrían for all of the great work on the preliminary ADE free molecular and DSMC analysis.

Without the influence of some incredible faculty, I can't imagine being in the position I'm in right now. I want to sincerely thank my advisor and the Director of the SFPL, Professor Dave Spencer, for being an amazing mentor and somehow always finding time to not only discuss challenges with me, but to also work through them with me; I doubt many other students can say that they had an advisor so involved and well organized. I want to thank Professor Alina Alexeenko for being an excellent instructor and for introducing me to the world of space flight projects with SASSI2, and also for providing valuable insight as a member of my committee. I also want to thank Professor Steven Collicott for serving on my committee and for helping to organize the course on spacecraft thermal analysis and design, my first class taken as a grad student. Additionally, thank you to Professor Dan Dumbacher for the incredible experience you provided through the study abroad courses you taught, and the wise advice you gave me as an undergrad when I was still figuring out what exactly I was planning to get out of grad school. Finally, thank you to Professor Tom Shih for taking time to help mentor me and expose me to the world of academic research while balancing doing an amazing job as the head of the AAE department.

My parents should get the most recognition, since I owe nearly everything to them and the sacrifices they've made to give me and my sister better lives. Momon and Baba, things turned out OK, huh? Sophie, let's keep it up, *kermenn*!

Lastly, shout-out to Andrew, Bob, Ceda, and David for being my go-to guys since basically forever.

TABLE OF CONTENTS

Page

LIST OF TABLES ix

LIST OF FIGURES x

ABSTRACT xii

1 INTRODUCTION 1

1.1 Contemporary relevance 2

1.2 6DOF modeling 4

1.2.1 Goals 6

2 MATHEMATICAL MODELS 8

2.1 Reference frame definitions 8

2.2 Geometry representation 10

2.3 Equations of motion 12

2.3.1 Translational motion 12

2.3.2 Rotational motion 14

2.4 Perturbations 19

2.4.1 Aerodynamics 20

2.4.2 Solar radiation pressure 27

2.4.3 Gravitational perturbations 32

2.5 Numerical method 34

2.6 DSMC 35

2.7 Additional considerations 35

3 APPLICATION - LIGHTSAIL 37

3.1 Mission description and Modeling considerations 37

3.2 6DOF simulation results 40

3.3 DSMC comparison 45

Page

3.4 Conclusions 47
4 APPLICATION - SAIL-BOOM-ROCKET 48
4.1 Mission description and Modeling considerations 48
4.2 6DOF simulation results 50
4.2.1 DSMC comparison 55
4.3 Conclusions 56
5 APPLICATION - AERODYNAMIC DEORBIT EXPERIMENT 57
5.1 Mission description and Modeling considerations 57
5.2 6DOF simulation results 61
5.3 DSMC comparison 65
5.4 Conclusions 66
6 CONCLUSION AND FUTURE WORK 68
6.1 Conclusion 68
6.2 Future Work 69
REFERENCES 71
A 6DOF SIMULATION USER'S GUIDE 75
A.1 Summary 75
A.2 How to Run a Simulation 77
A.2.1 Defining File Paths 77
A.2.2 Defining Geometry 77
A.2.3 Defining Spacecraft Properties 78
A.2.4 Miscellaneous Settings 79
A.2.5 Defining Time Settings 79
A.2.6 Defining Initial State 80
A.3 Simulation Logic 81
A.3.1 Mesh Generation 81
A.3.2 Propagation 81
A.3.3 6DOF Mode 82

Page

A.3.4 3DOF Mode 85
A.4 How to Add Perturbations 86
B SPARTA DSMC RUN PARAMETERS 87

LIST OF TABLES

Table Page

3.1 Lightsail 1 6DOF simulation initial conditions and parameters 39

3.2 Lightsail 1 DSMC aerodynamics comparison 47

4.1 SBR 6DOF simulation initial conditions and parameters 49

4.2 SBR DSMC aerodynamics comparison 56

5.1 ADE 6DOF simulation initial conditions and parameters 60

5.2 ADE DSMC aerodynamics comparison 65

A.1 6DOF Simulation function call breakdown 76

B.1 SPARTA DSMC Parameters 87

LIST OF FIGURES

Figure		Page
2.1	ECI, NTW, and body frames shown in relation to one another	9
2.2	Example of a simplified Aerodynamic Deorbit Experiment geometry represented through the STL file format	11
2.3	Example of rigid body rotation through the Euler axis principal: one vector defines an axis about which the body rotates	18
2.4	Modeling methods for different flow regimes	21
2.5	Surface element sample defining coordinates, velocity, and incidence angle	22
2.6	Sun position determination visualization, with the longitude and obliquity of the ecliptic shown	28
2.7	Earth shadow diagram, showing angles of penumbra and umbra	30
3.1	Lightsail geometry represented in STL format	38
3.2	Lightsail 1 simulated altitude history	40
3.3	Lightsail 1 simulated gravitational perturbation history	41
3.4	Lightsail 1 simulated orbital motion history	42
3.5	Lightsail 1 simulated combined total angular displacement from flow velocity vector based on yaw and pitch	43
3.6	Lightsail 1 simulated aerodynamic forces and torques	44
3.7	Lightsail 1 simulated solar radiation pressure forces and torques	45
3.8	Lightsail geometry (blue) and Lightsail geometry pitched by 30 degrees (red)	46
4.1	SBR geometry represented in STL format	48
4.2	SBR simulated combined total angular displacement from flow velocity vector based on yaw and pitch, 650 km case	50
4.3	SBR simulated aerodynamic perturbation history, 650 km case	50
4.4	SBR simulated gravitational perturbation history, 650 km case	51
4.5	SBR simulated solar radiation pressure perturbation history, 650 km case	51

Figure Page

4.6 SBR simulated combined total angular displacement from flow velocity vector based on yaw and pitch, 500 km case 52

4.7 SBR simulated aerodynamic perturbation history, 500 km case 52

4.8 SBR simulated gravitational perturbation history, 500 km case 53

4.9 SBR simulated solar radiation pressure perturbation history, 500 km case . 53

4.10 SBR simulated combined total angular displacement from flow velocity vector based on yaw and pitch, 450 km case 54

4.11 SBR simulated aerodynamic perturbation history, 450 km case 54

4.12 SBR simulated gravitational perturbation history, 450 km case 55

4.13 SBR simulated solar radiation pressure perturbation history, 450 km case . 55

5.1 Geosynchronous trasnsfer orbit geometry 58

5.2 ADE geometry represented in STL format 59

5.3 ADE simulated Euler angle history for first seven days after sail deployment 61

5.4 ADE simulated orbital altitude history for first seven days after sail deployment 61

5.5 ADE simulated Euler angle history for first seven days after sail deployment, zoomed in on a perigee pass 62

5.6 ADE simulated aerodynamic perturbation history for first seven days after sail deployment 63

5.7 ADE simulated aerodynamic perturbation history for first seven days after sail deployment, zoomed in on a perigee pass 63

5.8 ADE simulated gravitational perturbation history for first seven days after sail deployment 64

5.9 ADE simulated trajectory for first seven days after sail deployment 64

5.10 ADE simulated solar radiation pressure perturbation history for first seven days after sail deployment 64

5.11 Self shadowing diagram, showing how the simulation falsely identifies certain geometry downstream as "wetted" by the flow 66

ABSTRACT

Tamrazian, Sebastian MSAAE, Purdue University, May 2019. Development of a Coupled Orbit-Attitude Propagator for Spacecraft of Arbitrary Geometry. Major Professor: David A. Spencer.

The successful prediction of spacecraft motion is often heavily based upon assumptions used to simplify the problem without compromising solution accuracy. For many analyses, a primary assumption used is the decoupling of trajectory and attitude dynamics when calculating trajectories. In cases where spacecraft or objects have high area to mass ratios, non-conservative effects such as atmospheric drag and solar radiation pressure can greatly perturb spacecraft translational motion based on rotational state. A modular, six degree of freedom (6DOF) simulation with coupled orbit and attitude dynamics has been developed to model spacecraft and orbits of arbitrary geometries. First, the basis for the modular rotational and translational equations of motion are introduced. Next, formulations are provided for the gravity gradient torque, solar radiation pressure, aerodynamic, and non-spherical gravity potential sources of perturbations, and the Marshall Engineering Thermosphere atmospheric model used is described. A first test case is performed using the 6DOF simulation to simulate the deorbit of the spacecraft Lightsail 1, which flew in 2015. Next, predictive cases are demonstrated using the simulation for a theoretical sail-boom-rocket combination representative of a debris removal scenario, and for the Aerodynamic Deorbit Experiement, which will demonstrate a passively stable drag sail technology and characterize its effectiveness on orbit. All simulation cases have had aerodynamic perturbation formulations compared against high fidelity Direct Simulation Monte Carlo runs, and suggestions have been made for the future development of the simulation tool.

1. INTRODUCTION

For as long as we have been able to observe, we have attempted to predict. As in many branches of physics, successful state prediction in celestial mechanics is predicated on the careful application of assumptions and the selection of models that best represent the physical system. The assumptions made are dependent on the level of fidelity the analysis requires; the proper selection of assumptions can greatly reduce complexity while minimally reducing solution accuracy. In the orbital analysis of spacecraft, assumptions are often made in neglecting the perturbing effects of any number of physical phenomena. Relativistic effects, tidal gravitational perturbations, most n-body accelerations, and most higher order non-spherical gravity potential terms are frequently among the many possible sources of perturbing effects ignored. Of primary interest to this work is the common assumption that a trajectory can be analyzed while disregarding spacecraft attitude. For most traditional spacecraft applications where the area to mass ratio is low and attitude is strictly controlled, this three degree-of-freedom (3DOF) approach is valid. However, when considering objects or craft with high area to mass ratios, the coupling of attitude and trajectory can no longer be ignored, and a six degree-of-freedom (6DOF) analysis is necessary. In particular, the orientation of a spacecraft is a significant contributor to how solar radiation pressure (SRP), aerodynamics, and gravity gradient torques will perturb 6DOF motion.

Space debris is a topic that is closely tied to the orbital modeling of uncontrolled objects. At high Earth orbits such as geostationary orbit, damaged sheets of Multi Layer Insulation (MLI) flake off of large communications satellites and are easily perturbed by SRP, and the analysis of motion using 6DOF methods is necessary [1]. There is no universal definition at which an object is defined as having a high area to mass ratio, but the discovery of objects in orbit that are heavily perturbed by solar

radiation pressure at high orbits by Schildknecht [2–4] has led to increased interest in analyzing the effects of SRP on the trajectories of objects with area to mass ratios ranging from $0.1 m^2/kg$ to 20 m^2/kg. For Low Earth Orbit (LEO), the impact of a different area to mass ratio is very dependent on altitude. While solar radiation pressure force magnitudes are determined by the distance from the object in question and the sun, which is roughly 150 million kilometers at any Earth orbit, aerodynamic forces depend on the density of the immediate environment, which can vary greatly at different LEO altitudes. Although the study of motion for high area to mass ratio objects has been primarily concerned with space debris at higher orbits, planned high volume satellite constellations in LEO must expand the conversation to include lower orbits and subsequent aerodynamic effects as well.

At LEO, private enterprises are in the process of launching tens of thousands of small satellites in order to establish global communications networks [5–8]. With improper debris mitigation techniques and technologies, there exists a significant risk to the usability of certain orbits [9]. Of the many proposed technologies to reduce this space debris induced risk, drag sail technologies are perhaps among the most promising. By taking advantage of the rarefied gas environment in LEO, drag sails greatly increase a satellite's area to mass ratio and aerodynamic drag, allowing for an accelerated deorbit time line. For these craft, understanding of the attitude behavior concurrently with trajectory is critical, but is often neglected, as the traditional tools for the analysis of orbital motion are based on 3DOF models. This work is thus focused on developing an orbital propagation tool which accounts for the 6DOF motion of a body of arbitrary geometry while considering the effects of the rarefied aerodynamic environment, gravitational perturbations, and SRP.

1.1 Contemporary relevance

Satellite constellations can offer robust, modular, and dispersed solutions to global inter-connectivity. Companies such as SpaceX, Samsung, OneWeb, Boeing, and oth-

ers are looking to collectively place over 20,000 satellites in LEO to provide the global population with internet access [5–8]. These massive networks seek to provide a valuable service, but risk exacerbating the already precarious space debris situation in the high value orbits they will occupy. Although space debris has always been of some concern to the spaceflight community, the Iridium-Kosmos collision of 2009 demonstrated the real risk of a quickly accumulating debris field in LEO. Kessler first described the risk of forming a debris belt from the cascading effects of artificial satellite collisions, in a process analogous to that which formed the asteroid belt in our solar system, in 1978 [9]. Upon revisiting these theories in 2010, Kessler's conclusion was that the amount of debris in many critical orbits is already past the threshold of the 'Kessler Syndrome' cascading effect, and that there is a necessity to selectively deorbit large objects that are most likely to cause future debris through collisions [10]. Further, in order to prevent the growth of the debris cloud, there must be strict compliance with deorbit procedures designed to mitigate the amount of defunct spacecraft in critical orbits for extended periods of time [10].

Many technologies have been proposed for safe and effective spacecraft deorbit and debris mitigation. Thruster based mitigation methods are diverse and can be applied to a number of mission scenarios. The type of thruster required is dependent on the delta V necessary to deorbit; electric propulsion can provide superior efficiency when the extended time lines of deorbit are considered, while chemical propulsion can act more quickly to deorbit a craft [11]. A critical drawback is that the craft must be fully functional with working attitude control systems at the end of its mission, since the thrust must be directed on a specific vector for optimal deorbit. Electrodynamic tethers can also be used for deorbit by utilization of the Lorentz force, and can passively stabilize with gravity gradient torques. However, wires used for electrodynamic tethers, typically on the order of hundreds of meters or kilometers long, greatly increase collision likelihoods with other objects in LEO [10]. The final main approach of deorbit technologies is to alter the spacecraft ballistic coefficient. Reducing spacecraft mass and increasing effective area are both methods that lead

to a lower ballistic coefficient for a faster deorbit, however reducing spacecraft mass is difficult to do without introducing more debris into the environment [11]. Drag based approaches can be used passively without the requirement of active control, and designs have been developed for passive attitude stability using environmental torques [12, 13]. This drag based deorbit method is reliant on the fact that a rarefied atmosphere extends for over 1000 km past the surface of the Earth, and always imparts some aerodynamic drag on spacecraft in LEO. By greatly increasing a satellite's area to mass ratio, a drag sail works to magnify the effects of aerodynamics.

Just as a flat plate provides maximum drag when oriented perpendicular to a flow, a spacecraft with a drag sail has a similar maximum drag orientation, which is ideally passively maintained throughout the deorbit time line. In modeling the performance of a technology that perturbs translational motion based on its orientation relative to the environment, it becomes apparent that a coupled, 6DOF attitude and trajectory analysis must be used.

1.2 6DOF modeling

Many have explored the necessity of 6DOF simulation for spacecraft orbit propagation in various scenarios, however a generalized, modular simulation approach that calculates aerodynamic forces and torques analytically is yet unavailable. In the 1980s, concepts on large scale space structures, such as solar power farms and modular space stations began to gain interest after the end of the space race. For such structures, the combination of scale and mass is enough for gravity gradient torques to be of primary interest in understanding attitude behavior in orbit. Researchers understood that these torques are dependent on the orientation of the craft with respect to the attracting body, and so the necessity of coupled orbit and attitude became apparent. Sincarsin and Hughes incorporated higher order gravity gradient torque terms in a coupled orbit attitude framework inspired by these large orbital structures in 1983 [14]. More recently, coupled attitude and orbital analyses have been performed

for specific geometries in the context of relative spacecraft motion and control, again with a focus on gravity gradient torques [15,16]. Growing interest in the field of space debris has led many researchers to try to better understand how to best propagate the orbits of debris to determine how long objects could stay in orbit, and what kind of damage they may cause based on what orbits they cross. Much of this work has been done for high area to mass ratio objects, as in the work of Früh. Früh utilized a coupled orbit and attitude motion approach to analyze the effects of SRP on space debris in high orbits, and showed that attitude is significantly perturbed by SRP for high area to mass ratio debris, which then results in notable changes in long term trajectory modeling [17]. Further, Früh determined that the trajectory cannot safely be decoupled from the propagation of the orientation state for these objects being perturbed by SRP in high orbits; approximations based on averaged attitudes over specific time periods may be inadequate, and it was common for the simulated objects to end up in a rapidly rotating uncontrolled attitude state [18]. There are other cases where gravity gradient and SRP based torques are accounted for in a coupled simulation, but these analyses did not account for aerodynamic torques, as in [19] and [20].

Considerations for LEO

Now, with the effort spent developing drag sails, high area to mass ratio objects must also be considered in LEO, where aerodynamic effects are dominant. Many studies on specific drag sail technologies have been proposed with some form of aerodynamic modeling to validate system designs. Effective representation of the aerodynamic environment for satellite applications requires an understanding of the free molecular flow regime. Approaches have been detailed without utilizing the analytical equations for surface flux modeling derived for the regime, instead using, for example, a quasi-coupled effective drag area simplification. This approach also requires terms that must be determined uniquely each time a different spacecraft configura-

tion or orbit is used [21]. Roberts and Harkness derive forces and moments based on particle interaction, and subsequently propagate the motion of a conical drag sail spacecraft, but utilize a simplified 2D orbit while neglecting SRP and gravity gradient torques [12]. Long developed an analysis tool to characterize performance of the passively stable pyramid sail concept which takes into account the rarefied gas dynamic environment, SRP, and gravity gradient torques, but for a specific geometry, with minimal modularity, and exclusively for circular orbits [22]. POST2 is a tool developed by NASA for simulating point mass trajectories, but, refers to an aerodynamic database instead of determining aerodynamic forces and torques during simulation time for maximum accuracy [23]. To date, no modular, generalized, 6DOF propagation tool has been developed with attention to accurate modeling of the free molecular flow regime.

1.2.1 Goals

Trajectory perturbations for drag sail craft are heavily dependent on spacecraft orientation; a coupled orbit-attitude propagator is necessary to assess technology performance. The goal of this work is to develop a 6DOF propagator that is both fully modular, meaning it can be improved by incorporating more perturbations and complexity (and have specific perturbations removed at will), as well as non geometry specific, meaning any spacecraft geometry can be tested as provided by the user. Further, the propagator is to use accurate free molecular analytical equations to solve surface pressure and shear for determining aerodynamic forces and moments. These aerodynamic quantities will be evaluated against high fidelity Direct Simulation Monte Carlo (DSMC) method simulations. Finally, three spacecraft with high area to mass ratios will have their trajectories and behavior simulated using the propagator: Lightsail 1, which has already flown and will be used as a validation case, a Sail-Boom-Rocket (SBR) configuration proposed to deorbit spent rocket bodies, and the Aerodynamic Deorbit Experiement (ADE), which will flight test the passively stable

pyramid sail technology. Finally, recommendations will be made as to what aspects of the simulation could be improved upon for future refinement.

2. MATHEMATICAL MODELS

6DOF propagation of spacecraft motion is reliant upon correctly identifying reference frames, defining the spacecraft geometry that will be perturbed, using relevant equations of motion to propagate motion, and solving for perturbation sources to feed into the equations of motion. Initial state and spacecraft property data is also required, and is discussed as a set of inputs specific to each run case in subsequent chapters.

2.1 Reference frame definitions

There are three reference frames used in the 6DOF simulation. First, the spacecraft body frame is established as fixed in the spacecraft, translating and rotating with the spacecraft body such that a discrete point on the spacecraft is in a fixed location in space relative to the frame. This is used to define the tessellated surface geometry upon which force and torque calculations will be applied. Further, this body axis system is defined with the origin at the body center of mass, which allows for usage of the principal moments of inertia. This definition allows for simplified equations of motion as shown in Section 2.3.2. Second, a normal, tangential, cross-track (NTW) satellite frame is used to determine the spacecraft's angular displacement in orbit. The NTW frame shares an origin with the body frame, but is not fixed in the body; the frame rotates with the orbital position rather than the body it is centered on, and provides a reference to which the body frame can be compared. The NTW frame is also useful in that aerodynamic drag forces act directly opposite the tangent vector, since the tangent vector is aligned with the spacecraft velocity vector, and the frame is used as an intermediate step to convert from the body frame to the final frame used, Earth centered inertial (ECI). The ECI frame is used to represent the spacecraft translational displacement and the sun position for calculation of earth

shadowing and SRP. The ECI frame is located at the center of the Earth, and is an inertial frame that does not rotate with the rotation of the planet. The fundamental plane of the ECI system is defined by the equator, and the $\hat{x}$ direction is defined in the direction of the vernal equinox for a specific epoch, J2000.0. The body, NTW, and ECI frames are shown in relation with each other in Figure 2.1.

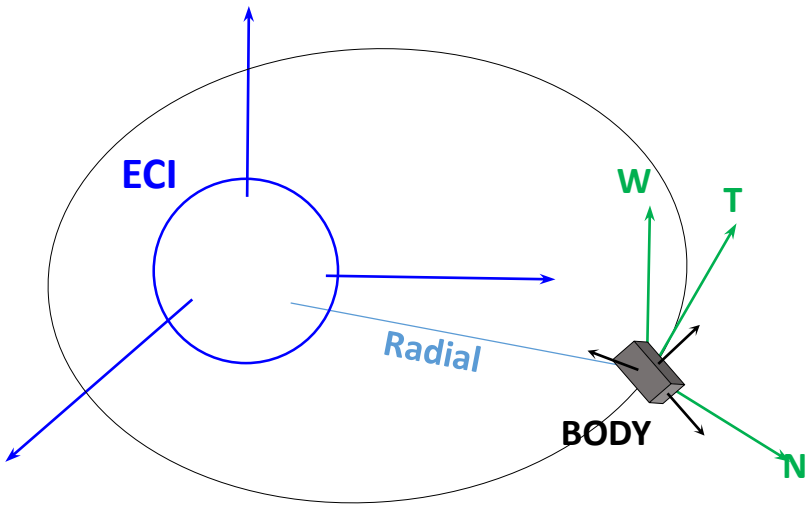

Fig. 2.1. ECI, NTW, and body frames shown in relation to one another

To convert between the body frame and NTW frame, a direction cosine matrix can be used. Here, a standard body 3-2-1 (roll pitch yaw) rotation order is used. The matrix is used such that $NTW = [DCM]BODY$. $C()$ represents the cosine of an angle, and $S()$ represents the sine. Here, roll is represented by ϕ, pitch is represented by θ, and yaw is represented by ψ. The matrix is shown below in (2.1) [24].

$$\begin{bmatrix} C(\phi)C(\theta) & C(\phi)S(\theta)S(\psi) - C(\psi)S(\phi) & C(\phi)S(\theta)C(\psi) + S(\psi)S(\phi) \\ S(\phi)C(\theta) & S(\phi)S(\theta)S(\psi) + C(\psi)C(\phi) & S(\phi)S(\theta)C(\psi) - S(\psi)C(\phi) \\ -S(\theta) & C(\theta)S(\psi) & C(\theta)C(\psi) \end{bmatrix} \tag{2.1}$$

Representing the relationship between the NTW and ECI frames requires the spacecraft position and velocity vectors. The fact that the tangential T component

is aligned with the spacecraft orbital velocity can be used here, and then the out of plane, orthogonal W component can be found using a cross product. The final, in plane normal component N completes the right handed set. The relations can be found in Equation set (2.2).

$$\begin{aligned} \hat{T} =& \frac{\vec{v}}{|\vec{v}|} \\ \hat{W} =& \frac{\vec{r} \times \vec{v}}{|\vec{r} \times \vec{v}|} \\ \hat{N} =& \hat{T} \times \hat{W} \end{aligned} \tag{2.2}$$

2.2 Geometry representation

In order to determine the environmental effects on the rotational state of the spacecraft, a model for geometry must be developed. Since the goal of the propagator is to be generally applicable, a standard file format that presents the geometry in a method that allows for calculation of imparted surface momenta is preferred. Specifically, as will be seen in the following sections on perturbation sources, a polygonal representation of the geometry surface that allows for the calculation of surface element areas and surface normal unit vectors is desired. The .STL file format [25], which uses stereolithography techniques patented by Hull in 1986 [26], provides a triangular mesh of the surface defined by a list of vertices and normal vectors. An example geometry represented through the .STL file format is shown in Figure 2.2.

If the pressure and shear are known on a surface, the area can be used to provide the total force, and the vector from the center of mass to the centroid of the surface element can be used to determine the moment. Summed over all surface elements, these individual forces and torques can be used to find the total imparted perturbation from an environmental effect, for example aerodynamics or SRP. Finding the centroid,

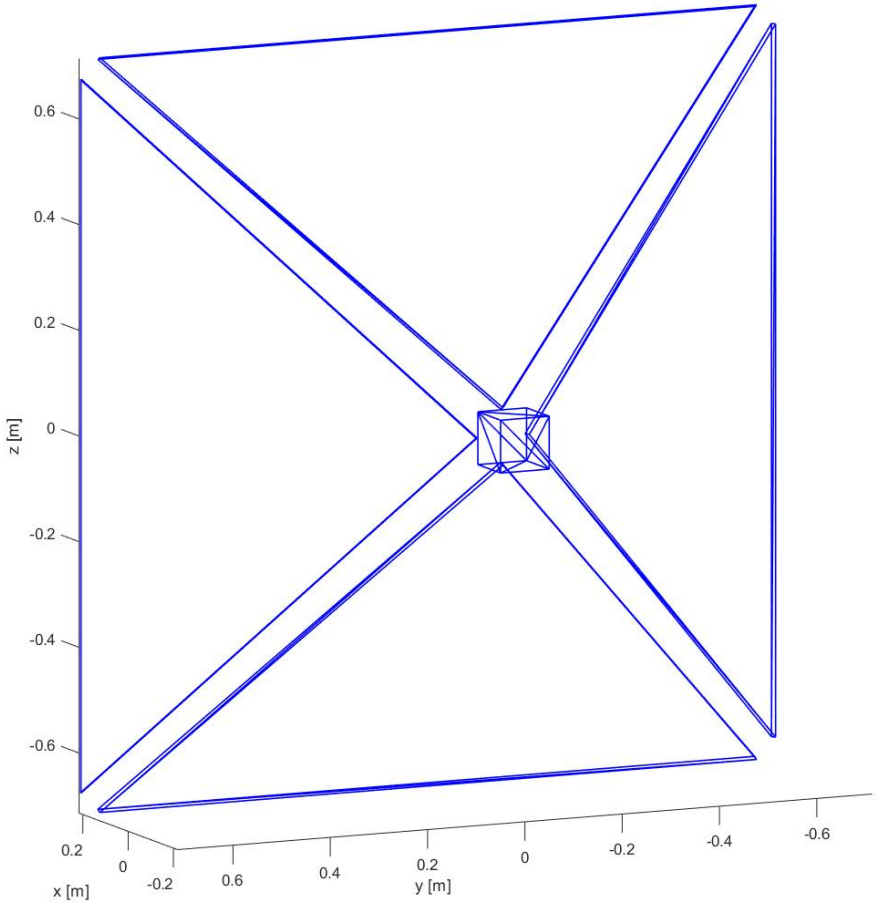

Fig. 2.2. Example of a simplified Aerodynamic Deorbit Experiment geometry represented through the STL file format

C, of a triangle in 3D space is simple, as shown in Equation (2.3) for a triangle with vertices i, j, k.

$$(C_x, C_y, C_z) = \frac{1}{3}[(i_x, i_y, i_z) + (j_x, j_y, j_z) + (k_x, k_y, k_z)] \tag{2.3}$$

The area of a triangle can be found using Heron's formula, known to the ancients. If the lengths of the sides of a triangle are known as a, b, c, and half of the perimeter

(the semi-perimeter) of the triangle is s, then the triangle area is found as shown in Equation (2.4)

$$A = \sqrt{s(s-a)(s-b)(s-c)} \tag{2.4}$$

With the area, centroid, and normal vector of each surface element, pressure and shear effects from the environment can be used to determine the effect on the 6DOF motion of the spacecraft by applying them to the equations of motion, discussed next.

2.3 Equations of motion

The equations of motion used for the propagation of spacecraft motion must be generic such that any elliptical orbit geometry and any number of perturbations can be accounted for. The differential equations of motion apply either to translational or rotational motion. For rotation, the dynamic equations of motion are used to determine angular rates based off of perturbing torques, while the kinematic equations of motion use these angular rates to determine the orientation state. In this work, special perturbation techniques are used to resolve the motion, resulting in a formulation that can easily be modified to include other perturbations. The coupled nature of the problem does not lend itself well to general perturbation analysis for the host of external forces being considered. In particular, Cowell's formulation is used to model orbital motion, while Euler parameters (quaternions) are used as the kinematic variables used to resolve the rotational state using the dynamic and kinematic equations of motion.

2.3.1 Translational motion

As described in Battin [27], Cowell's formulation is the simplest way to determine the translational state of an orbiting body in a Cartesian coordinate system when the motion is non-Keplerian. Cowell, along with Cromellin, first utilized this approach as a numerical method to predict the motion of Halley's comet, based on numerical inte-

gration methods first described by Gauss [28]. The formulation affords the inclusion of any number of linearly summed perturbing accelerations, such that the resulting $a_{perturbing}$ captures the effects that cause the trajectory to deviate from the two body Keplerian motion. Cowell's formulation is shown in Equation (2.5).

$$\ddot{\vec{r}} = -\frac{\mu}{r^3}\vec{r} + \vec{a}_{perturbing} \tag{2.5}$$

Here, on the left hand side $\ddot{\vec{r}}$ represents the second time derivative of the position vector of the craft: the acceleration, or specific force. The standard gravitational paremeter of the central body is represented by μ, r represents the distance magnitude of the orbiting body to the origin of the central body, and $\vec{r}$ represents the position vector of the craft from the same origin. All translational perturbations are captured by the $a_{perturbing}$ term. As long as a calculation is performed to determine an acceleration on the orbiting body for some force, conservative or non-conservative, for the instantaneous state, any number of these accelerations can be summed to determine a net acceleration on the craft which will deviate it from the Keplerian orbit. In the case of this work, perturbations from an non-spherical gravity potential model (J_2 effects), SRP, and aerodynamics are considered, such that the $a_{perturbing}$ can be described as in Equation (2.6).

$$\vec{a}_{perturbing} = \vec{a}_{J_2} + \vec{a}_{SRP} + \vec{a}_{Aero} \tag{2.6}$$

Upon integration of (2.5) using the accelerations in (2.6), the new position and velocity can be determined in Cartesian coordinates for the specified timestep. Brouwer and Clemence [29] note how for this method a small integration step is necessary as the integration is slowly convergent. The original way in which Cowell numerically integrated (2.5) is known as Cowell's method. With contemporary computational advances, there are many ways to integrate the equation of motion. In the case of this simulation, a variable time step integrator is utilized to meet a specified solver tolerance, as discussed in Section 2.5.

2.3.2 Rotational motion

Successful determination of the rotational state for this work utilizes a set of dynamic equations of motion, and a set of kinematic equations of motion. The dynamic equations of motion relate the body torques to angular rates based on the inertia properties of the body. Using these angular rates, the kinematic equations of motion, in this case using quaternions, are used to determine the orientation state of the spacecraft.

Dynamic equations of motion

The dynamic equations of motion will be used to determine the body angular rates based on the body torques and spacecraft inertia properties. The two frames necessary for this derivation are the body centered NTW frame (does not rotate with the body), and the body fixed frame (rotates with the body), both with origins at the body center of mass. Let $\hat{b}_i$ represent the body fixed frame unit vectors, $\hat{a}_i$ represent the NTW frame unit vectors, and B^* represent the body center of mass. Assume an arbitrary body mass distribution, such that the inertia dyadic in the body frame at the center of mass is represented by Equation (2.7).

$$\bar{\bar{I}}^{b/B^*} = I\hat{b}_1\hat{b}_1 + J\hat{b}_2\hat{b}_2 + K\hat{b}_3\hat{b}_3 \tag{2.7}$$

Here, I, J, and K represent the principal inertias of the spacecraft. The formulation is general and there is no assumption on symmetry of mass distribution. Since the body frame and NTW frame share an origin, only rotational displacements separate the two. A set of angular velocities, represented by ${}^a\bar{\omega}^b$ can be used to quantify the rates of these displacements, as in Equation (2.8).

$${}^a\bar{\omega}^b = \omega_1\hat{b}_1 + \omega_2\hat{b}_2 + \omega_3\hat{b}_3 \tag{2.8}$$

Finally, consider some arbitrary torque defined with the body axes, which will represent the perturbing torques from the spacecraft environment. This moment can be represented as shown in Equation (2.9).

$$\overline{M}^{B^*} = M_1\hat{b}_1 + M_2\hat{b}_2 + M_3\hat{b}_3 \tag{2.9}$$

In a rotational context, the moment of inertia is analogous to linear inertia, represented by mass, just as angular velocity is analogous to linear velocity. In a linear context, momentum is the product of mass and velocity. As such, the *angular* momentum of the body in the $\hat{a}$ frame is the product of the inertia tensor and angular velocities shown in Equation (2.10).

$${}^a\overline{H}^{B^*} = \bar{\bar{I}}^{b/B^*}{}^a\bar{\omega}^b \tag{2.10}$$

Again, in a linear context, the specific acceleration, or force, is equal to the first time derivative of the linear momentum. Here, the moment is equivalent to the first time derivative of angular momentum. Since this analysis is in a rotating environment, special care must be taken to preserve the correct frame representations for the terms. By expanding this relation, the dynamic equations of motion for the rotating system can be found. The relation is shown in Equation (2.11).

$$\overline{M}^{B^*} = \frac{{}^a d^a\overline{H}^{B^*}}{dt} \tag{2.11}$$

The first step is to expand the dyadic form in Equation (2.10). Expanding the dyadic using Equation (2.7) and Equation (2.8) gives Equation (2.12).

$$\begin{aligned} {}^a\overline{H}^{B^*} &= (I\hat{b}_1\hat{b}_1 + J\hat{b}_2\hat{b}_2 + K\hat{b}_3\hat{b}_3)(\omega_1\hat{b}_1 + \omega_2\hat{b}_2 + \omega_3\hat{b}_3) \\ &= I\omega_1\hat{b}_1 + J\omega_2\hat{b}_2 + K\omega_3\hat{b}_3 \end{aligned} \tag{2.12}$$

Notice that the angular momentum is given in terms of the body frame. In order to take the derivative of this quantity in the NTW frame while keeping the body

frame representation, the basic kinematic equation must be used, which uses the relationship between the body and NTW frames previously established through the angular velocities in Equation (2.8). This formulation is given in Equation (2.13).

$$\frac{{}^{a}d^{a}\overline{H}^{B^*}}{dt} = \frac{{}^{b}d^{a}\overline{H}^{B^*}}{dt} + {}^{a}\bar{\omega}^{b} \times {}^{a}\overline{H}^{B^*} \tag{2.13}$$

Using Equation (2.12) and Equation (2.8) in Equation (2.13) gives Equation (2.14).

$$\begin{aligned}\frac{{}^{a}d^{a}\overline{H}^{B^*}}{dt} =& I\dot{\omega}_1\hat{b}_1 + J\dot{\omega}_2\hat{b}_2 + K\dot{\omega}_3\hat{b}_3 \\ &+ \omega_1 J\omega_2\hat{b}_3 - \omega_1 K\omega_3\hat{b}_2 \\ &- \omega_2 I\omega_1\hat{b}_3 + \omega_2 K\omega_3\hat{b}_1 \\ &+ \omega_3 I\omega_1\hat{b}_2 - \omega_3 J\omega_2\hat{b}_1\end{aligned} \tag{2.14}$$

Recalling the relation between angular momentum and the moment as in Equation (2.11), and then simplifying the right hand side of Equation (2.14), the relation between the moment and angular rates is found, which is a form of the dynamic equations of motion. This can further be adjusted by grouping terms expressed in the same body direction, as in Equation (2.15).

$$\begin{aligned}\overline{M} =& [I\dot{\omega}_1 + K\omega_2\omega_3 - J\omega_3\omega_2]\hat{b}_1 \\ &+ [J\dot{\omega}_2 + I\omega_3\omega_1 - K\omega_1\omega_3]\hat{b}_2 \\ &+ [K\dot{\omega}_3 + J\omega_1\omega_2 - I\omega_2\omega_1]\hat{b}_3\end{aligned} \tag{2.15}$$

Finally, solving for the angular rate derivatives in Equation (2.15) and simplifying gives the dynamic equations of motion, shown in Equation set (2.16).

$$\begin{aligned}\dot{\omega}_1 =&[(J-K)\omega_2\omega_3 + M_1]/I \\ \dot{\omega}_2 =&[(K-I)\omega_1\omega_3 + M_2]/J \\ \dot{\omega}_3 =&[(I-J)\omega_1\omega_2 + M_3]/K\end{aligned} \tag{2.16}$$

These dynamic equations of motion relate the angular rates to an arbitrary moment. The most important aspect of these equations is that they are generalized, meaning there are no assumptions regarding what axes the torques act upon, or how the mass is distributed in the spacecraft. The M_i terms represent the summation of all torques imparted on the spacecraft. Similar to how the accelerations from different sources were summed to provide the total perturbing acceleration in Equation (2.6), the summation of the perturbing torques can be captured using Equation (2.17).

$$\overline{M} = M_{GravityGradient} + M_{SRP} + M_{Aero} \tag{2.17}$$

Now, a relation between the moments on the craft and the craft angular rates has been established. In Section 2.4, the calculations to determine these torques are shown. Next, a relationship must be established between the dynamic equations of rotational motion and the spacecraft orientation and the body angles used to represent the spacecraft attitude state.

Kinematic equations of motion

The kinematic equations of motion are used to describe the attitude state of the spacecraft based on the angular rates that the dynamic equations of motion provide. Many different methods of representing the kinematic equations of motion exist, but for spacecraft application, Euler parameters, or quaternions, are often

used. Euler first derived formulae for the rotation of arbitrary rigid bodies using one axis and rotation, as in Figure 2.3, from which any orientation could be accomplished [30]. Hamilton first described a four dimensional non commutative system he called quaternions [31] in 1843. A self described pure mathematician, many of Hamilton's discoveries are now of great importance in physics, with quaternions being no exception.

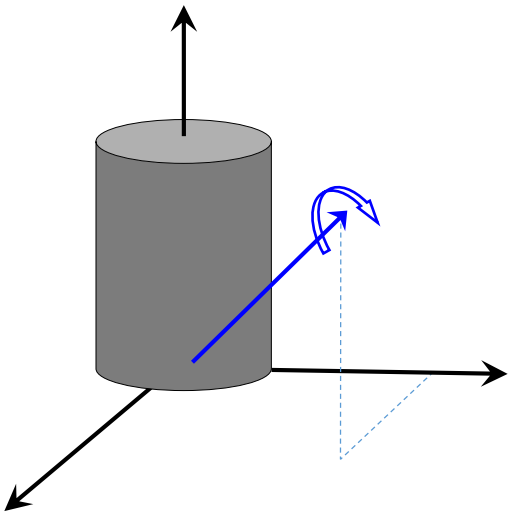

Fig. 2.3. Example of rigid body rotation through the Euler axis principal: one vector defines an axis about which the body rotates

By representing the concept of the Euler axis rotation using quaternions (three components in a vector form to define the axis, one scalar component to define the rotation), the arbitrary rotation of a rigid body can be performed without reliance on trigonometric functions which can produce singularities and reduce computational efficiency. Skylab is an example of a spacecraft which used quaternions for attitude modeling to explicitly avoid these singularities [32]. Wie mentions how the use of quaternions instead of Euler angles is now preferred in spacecraft dynamical modeling, especially for on-board operations and state determination, due to reduced computational requirements [24]. The use of quaternions in this context of rigid body

rotations was developed independently by Robinson, Harding, Mortensen, and Marguiles [?, 33–36]. The derivation is described in detail in the provided references, and results in the following kinematic equations of motion, shown in Equation set (2.18).

$$\begin{aligned}
\dot{q}_1 &= (\omega_1 q_4 - \omega_2 q_3 + \omega_3 q_2)/2 \\
\dot{q}_2 &= (\omega_1 q_3 - \omega_2 q_4 + \omega_3 q_2)/2 \\
\dot{q}_3 &= (-\omega_1 q_2 - \omega_2 q_1 + \omega_3 q_4)/2 \\
\dot{q}_4 &= -(\omega_1 q_1 - \omega_2 q_2 + \omega_3 q_3)/2
\end{aligned} \tag{2.18}$$

Here, the vector component is q_{1-3}, and the scalar component is q_4. With this formulation, the angular rates determined in the dynamic equations of motion in Equation set (2.16) can be related to the orientation state of the body using quaternions. By integrating these equations, the spacecraft attitude at an instance in time can be found from the result of some arbitrary perturbing torque.

2.4 Perturbations

Now that the equations of motion governing the craft's 6DOF motion have been established, the perturbations that will feed into those equations must be introduced. As previously mentioned, and shown in Equations (2.6) and (2.17), the perturbations considered for this analysis are gravity gradient torques, Earth oblateness accelerations, SRP forces and torques, and aerodynamic forces and torques. In the following sections, the determinations of these forces and torques in the context of the 6DOF simulation will be explained.

2.4.1 Aerodynamics

In order to properly model the aerodynamic forces in the simulated environment, there must be an understanding of the applicable aerodynamic flow regime. Although there has been study of rarefied gas dynamics since the late 1800s, the mid 20th century brought about new thinking as a result of the great advances in high altitude flight. Whereas much previous study was focused on the applicability to rarefied gas dynamics in the context of a vacuum type chamber or some type of internal interaction, there was now an interest in determining the effects of rarefied gas dynamics on 'submerged' bodies, for example a very high altitude craft experiencing atmospheric drag [37]. There was significant work done around this time to then characterize and categorize aerodynamic regimes. Based on this work from the mid century, all aerodynamic modeling can be divided into three flow regimes: free molecular flow, transitional flow, and continuum flow. Sometimes, a category known as 'slip flow' is used to describe the regime between continuum and transitional, but this regime is not relevant to this work.

Flow regimes

The categorization of the flow regime can be based on the degree of flow rarefaction, modeled by the non-dimensional Knudsen number. The Knudsen number is the ratio between the average distance between molecular collisions in the freestream, and a characteristic length of the body being modeled in the flow. This nondimensional quantity is given by Equation (2.19).

$$Kn = \frac{\lambda}{L} \tag{2.19}$$

Here, λ represents the molecular mean free path, which is the average distance between particle collisions in the flow, and L is the characteristic length of the body being modeled. A high Knudsen number, ($Kn >> 1$), corresponds to a free molecular

flow [38]. An overview of the modeling techniques applicable to each flow regime is recreated in Figure 2.4 here from Bird [39].

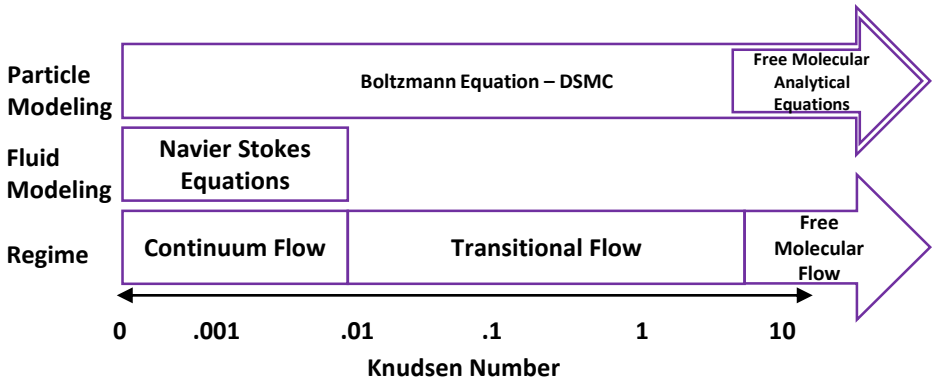

Fig. 2.4. Modeling methods for different flow regimes

It can be seen that the Navier stokes equations typically used in computational fluid dynamics cannot be used for high Knudsen numbers, since the approximation that the flow acts as a fluid is no longer applicable. Here, the discrete particle nature of the gas must be taken into account. For all flow regimes, the Boltzmann transport equation is able to capture the physics of the flow. However, this approach is extremely computationally intensive, and is not suitable to run on the timesteps required for 6DOF modeling on a spacecraft in orbit. The DSMC method was first proposed by Bird in 1963 [40], and is discussed in Section 2.6. For the case of a spacecraft in orbit, however, the flow regime is dominantly free molecular flow, and certain assumptions can be made to greatly simplify the calculation of aerodynamic forces on a body. In particular, particles are assumed to not collide with each other in the flowfield for free molecular flow. The significance here is that there is no flowfield to resolve; only surface interactions are relevant. Gombosi describes this by saying that the molecules travel such a relatively long distance between a surface collision

and a second collision with an incoming particle, that there is no shock wave ahead of a body in the free molecular flow regime [38]. In fact, the boundary layer is expected to be extremely diffuse and have no effect on the incident flow. A consideration to make here is that free molecular flow is not necessarily suited well for concave bodies, since particles may reflect off of a surface back onto a different surface, which is not inherently taken into account. Determination of the level of validity to which the free molecular models recreate the true flow can be done with DSMC modeling, and is discussed for specific geometries in the following chapters.

Free molecular aerodynamic force modeling

Schaaf and Chambré outline the method to determine aerodynamic forces on a surface [41], and their formulations guided the development of the free molecular interaction model for the spacecraft used in this work. First, consider a surface element in 3D space as shown in Figure 2.5.

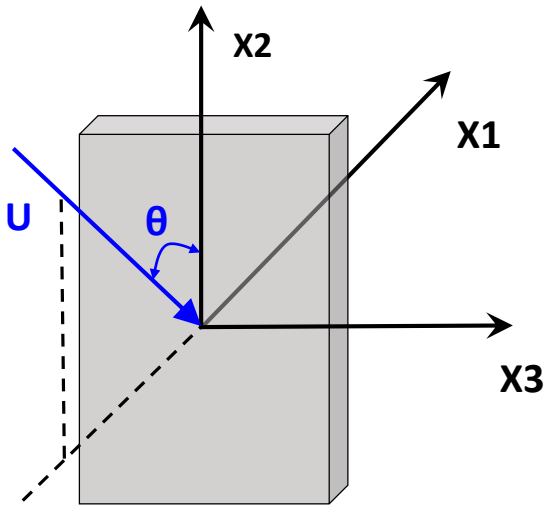

Fig. 2.5. Surface element sample defining coordinates, velocity, and incidence angle

It has been shown through experiment [42] that a singular accommodation coefficient, used to model the expected ratio between diffuse and specular particle reflections on a surface, can be insufficient for determination of certain surface fluxes. For the force modeling, consider two different accommodation coefficients, one describing the tangential interaction, and one describing the normal interaction, as shown in Equation set (2.20),

$$\begin{aligned} \sigma &= \frac{\tau_i - \tau_r}{\tau_i - \tau_w}, (\tau_w = 0) \\ \sigma' &= \frac{p_i - p_r}{p_i - p_w} \end{aligned} \tag{2.20}$$

Here, the subscript i refers to incident flux, r refers to the reflected flux, and w represents the flux of the particles remitted with a Maxwellian distribution at the surface temperature of the body with which they collide. The letters σ and τ represent the tangential components, while σ' and p represent the normal components. An assumption is made where the velocity of the molecules in the flow follows a Maxwellian distribution in order to determine the number density. Using the same coordinates defined in Figure 2.5 to describe the absolute velocity components v_{1-3}, the number density, f, per unit volume can be given by Equation (2.21).

$$f = \frac{\rho_\infty}{m(2\pi RT_\infty)^{3/2}} exp\left[-\frac{(v_1 - U\sin(\theta)^2 + (v_2 + U\cos(\theta))^2 + v_3^2}{2RT}\right] \tag{2.21}$$

Here, m represents the averaged molecular mass of the flow, R represents the specific gas constant, T_∞ represents the freestream temperature, θ is the incidence angle as shown in Figure 2.5, ρ_∞ is the freestream density, and U is the steady gas velocity. This can be used to determine the incident number of molecules on a surface element of area dA per unit time, modeled in Equation (2.22).

$$N_i = \int_{-\infty}^{\infty}\int_{-\infty}^{\infty}\int_{0}^{\infty} v_1 f dv_1 dv_2 dv_3 dA \tag{2.22}$$

Integrating this using the number density function given in Equation (2.21) gives Equation (2.23).

$$N_i = \frac{\rho_\infty}{m}\sqrt{\frac{RT}{2\pi}}[exp(-(s*\sin(\theta))^2) + \sqrt{\pi}(s*\sin(\theta))(1+erf(s*\sin(\theta)))]dA \quad (2.23)$$

Where $erf()$ represents the error function, and s is the molecular speed ratio, defined by the ratio between the bulk gas velocity and random thermal motion of the constituent flow particles, as in Equation (2.24).

$$s = \frac{U}{\sqrt{2RT}} \quad (2.24)$$

Equation (2.23) is general and can be used to determine energy flux and heat transfer. Building off of this can also give the formulation for the normal and tangential incident stresses on the surface (pressure and shear), shown in Equation set (2.25). Here, the solution of each integral is listed beneath each relevant equation.

$$p_i = \int_{-\infty}^{\infty}\int_{-\infty}^{\infty}\int_{0}^{\infty} mv_1^2 f dv_1 dv_2 dv_3 dA$$

$$p_i = \frac{\rho_\infty U^2}{2\sqrt{\pi}s^2}\left[(s*\sin(\theta))exp(-(s*\sin(\theta))^2) + \sqrt{\pi}[\frac{1}{2} + (s*\sin(\theta))^2][1+erf(s*\sin(\theta))\right]$$

$$\tau_i = \int_{-\infty}^{\infty}\int_{-\infty}^{\infty}\int_{0}^{\infty} mv_1 v_2 f dv_1 dv_2 dv_3 dA$$

$$\tau_i = -\frac{\rho_\infty U^2\cos(\theta)}{2\sqrt{\pi}s}\left[exp(-(s*\sin(\theta))^2) + \sqrt{\pi}(s*\sin(\theta)[1+erf(s*\sin(\theta))]\right] \quad (2.25)$$

To find the total pressure and shear, the reflected components, p_r and τ_r, must also be accounted for. These can be obtained using the definitions of the accommodation coefficients from Equation (2.20), resulting in Equation set (2.26).

$$
\begin{aligned}
p_r =& (1-\sigma')p_i + \sigma' p_w, p_w = \frac{1}{2} m \sqrt{2\pi R T_w} N_i \\
\tau_r =& (1-\sigma)\tau_i \\
p =& (p_i + p_r) \\
\tau =& (\tau_i - \tau_r)
\end{aligned}
\tag{2.26}
$$

With T_w representing the surface wall temperature, and N_i coming from Equation (2.23). Using Equation sets (2.25) and (2.26), the total pressure and shear values on the surface can be found, shown in Equation set (2.27)

$$
\begin{aligned}
p =& \frac{\rho_\infty U^2}{2s^2} \Bigg[\left(\frac{2-\sigma'}{\sqrt{\pi}} s * \sin(\theta) + \frac{\sigma'}{2} \sqrt{\frac{T_w}{T_\infty}} \right) exp(-(s * \sin(\theta))^2) \\
& + \left[(2-\sigma')[(s * \sin(\theta))^2 + \frac{1}{2}] + \frac{\sigma'}{2} \sqrt{\frac{T_w \pi}{T_\infty}} (s * \sin(\theta)) \right] [1 + erf(s * \sin(\theta))] \Bigg]
\end{aligned}
$$

$$
\tau = - \frac{\sigma \rho_\infty U^2 \cos(\theta)}{2\sqrt{\pi}} \left[exp(-(s * \sin(\theta))^2) + \sqrt{\pi} (s * \sin(\theta)) [1 + erf(s * \sin(\theta))] \right]
\tag{2.27}
$$

By applying the Equations in (2.27) to a surface element that is a component of the total spacecraft geometry, the local pressure and shear can be found. As seen in Hart [43], it can be convenient to non-dimensionalize these equations to obtain pressure and shear coefficients. This non-dimensional form is shown in Equation set (2.28).

$$C_p = \frac{1}{s^2}\left[\left(\frac{2-\sigma'}{\sqrt{\pi}} s*\sin(\theta) + \frac{\sigma'}{2}\sqrt{\frac{T_w}{T_\infty}}\right) exp(-(s*\sin(\theta))^2) + \left[(2-\sigma')[(s*\sin(\theta))^2 + \frac{1}{2}] + \frac{\sigma'}{2}\sqrt{\frac{T_w \pi}{T_\infty}}(s*\sin(\theta))\right][1 + erf(s*\sin(\theta))\right]$$

$$C_\tau = -\frac{\sigma\cos(\theta)}{s\sqrt{\pi}}\left[exp(-(s*\sin(\theta))^2) + \sqrt{\pi}(s*\sin(\theta))[1 + erf(s*\sin(\theta))]\right] \tag{2.28}$$

The coefficients of pressure and shear can then be summed by converting them to vector form using the normal and tangential unit vectors of the surface element. This is shown in Equation (2.29).

$$C_F = \left[C_p(\hat{normal}) + C_\tau(\hat{tangential})\right] \tag{2.29}$$

Using this intermediate 'force coefficient', the total force and moment can be found on the craft by summing over all elements i as in Equation set (2.30).

$$\vec{F}_{Aero} = \frac{1}{2}\rho_\infty U^2 \left(\sum C_{F,i} A_i\right)$$

$$\vec{a}_{Aero} = F_{Aero}/m \tag{2.30}$$

$$\vec{M}_{Aero} = \frac{1}{2}\rho_\infty U^2 \left[\sum \vec{r}_{cm,i} \times (C_{F,i} A_i)\right]$$

Here, the spacecraft mass is represented by $m_{s/c}$ and is used to find the acceleration on the body, which will be used to propagate orbital motion. The moment is also found using the force, with $r_{cm,i}$ representing the vector between the spacecraft center of mass and the centroid of the surface element. With this moment and acceleration, the 6DOF motion due to aerodynamics can be found. Note that to propagate this

correctly based on the equations of motion previously defined, the acceleration must be represented in the ECI frame, and the torque must be represented in the body frame. The force is represented in the NTW frame, so conversions using the relations in Section 2.1 are necessary.

Atmospheric modeling

Selection of the atmospheric model can be as important as the selection of the force model. In this work, a version of the Marshall Engineering Thermosphere (MET) model has been used, as translated from FORTRAN 77 to MATLAB by Long [22]. The model itself is a modified Jacchia 70 atmospheric model, and is a semi-empirical model that is based on satellite drag analyses [44]. The model is particularly useful due to the fact that it can be used to calculate approximate species concentrations and freestream temperatures in the exosphere, which can be used to determine properties required by the free molecular analytical equations. The model uses solar flux and geomagnetic index values as inputs, which are available through the NASA Marshall Space Flight Center solar activity forecast from the Natural Environments Branch as well [45]. Note that the forecast for these values changes over time as new data becomes available to researchers, and so for propagation at future epochs, the most up to date forecast values should be used.

2.4.2 Solar radiation pressure

Modeling the solar radiation pressure is similar to modeling the aerodynamics, in that force is calculated for each discrete element of the surface geometry. However, sun vector information and Earth shadow geometry information are also necessary.

Sun position determination

As the Earth revolves around the Sun, the vector from which sunlight is directed varies throughout the year. To determine the effects of SRP on a spacecraft, the direction from which incoming photons are coming must first be ascertained. For this work, a simple approximate model is used to determine the Sun position vector as described in the 1992 Astronomical Almanac [46]. The formulation allows a simple algorithm to replace the need for high accuracy ephemerides or Earth orbit propagation while retaining an accuracy of 0.01^o from 1950 to 2050, with loss of accuracy past these dates due to truncation error inherent in the approximation [47].

Beginning with an initial epoch for propagation, the Julian date, in the form of Julian centuries, is used to find the mean longitude and mean anomaly, the ecliptic longitude, obliquity of the ecliptic, and magnitude of the Earth Sun distance. An example of the geometry is shown in Figure 2.6, where the direction of the first point of Aries (vernal equinox) is denoted as Υ.

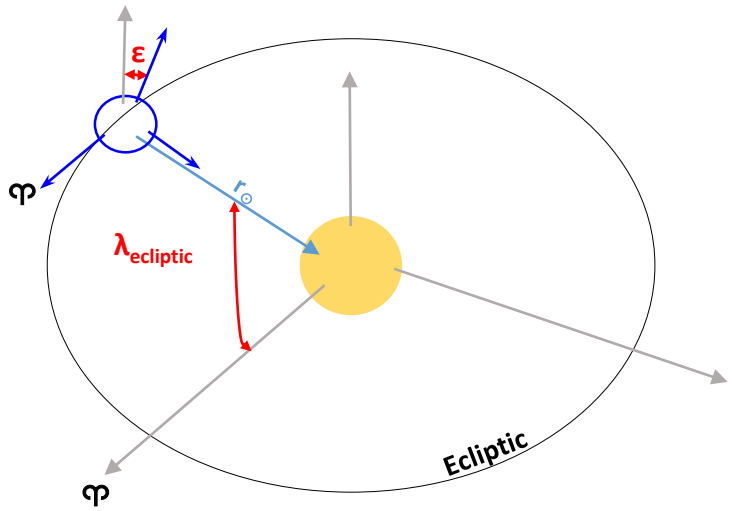

Fig. 2.6. Sun position determination visualization, with the longitude and obliquity of the ecliptic shown

The formulation is demonstrated in Equation set (2.31), with JC representing Julian centuries, λ_M representing mean longitude, M representing mean anomaly, $\lambda_{ecliptic}$ representing ecliptic longitude, and ϵ representing the obliquity of the ecliptic.

$$\begin{aligned} \lambda_M &= 280.46 + 36000.771 * JC \\ M &= 357.5291092 + 35999.05034 * JC \\ \lambda_{ecliptic} &= \lambda_M + 1.914666471 * \sin(M) + .019994643 * \sin(2M) \\ r_\odot &= 1.000140612 - .016708617 * \cos(M) - .000139589 * \cos(2M) \\ \epsilon &= 23.439291 - .0130042 * JC \end{aligned} \tag{2.31}$$

$$\vec{r}_\odot = \begin{bmatrix} r_\odot \cos(\lambda_{ecliptic}) \\ r_\odot \cos(\epsilon) \sin(\lambda_{ecliptic}) \\ r_\odot \sin(\epsilon) \sin(\lambda_{ecliptic}) \end{bmatrix}$$

Earth shadow

For many orbits without very high inclinations, the orbiting spacecraft will enter the shadow cast by the Earth, either fully or partially negating any effects of SRP. Figure 2.7 demonstrates the geometry of the Earth Sun shadow that can be used to determine if the satellite is in Earth's umbra or penumbra.

The umbra and penumbra shadow angles can be calculated by using right triangle relations as demonstrated in Vallado [47]. The formulation is shown in Equation set (2.32), with $R_\odot$ and $R_\oplus$ representing the Sun and Earth radii, respectively.

$$\begin{aligned} \alpha_{umbra} &= \frac{R_\odot - R_\oplus}{r_\odot} \\ \alpha_{penumbra} &= \frac{R_\odot + R_\oplus}{r_\odot} \end{aligned} \tag{2.32}$$

Next, the angular separation between the satellite and sun vector must be determined, which can be done using the dot product as shown in Equation (2.33).

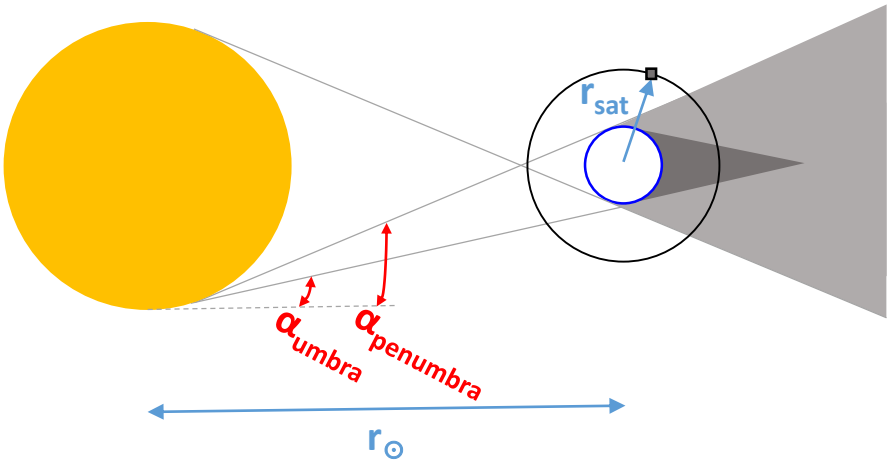

Fig. 2.7. Earth shadow diagram, showing angles of penumbra and umbra

$$cos(\phi) = \frac{\vec{r}_{\odot}\vec{r}_{sat}}{r_{\odot}r_{sat}} \tag{2.33}$$

Using the values from Equation set (2.32) and Equation (2.33), the satellite can be determined to either be in the umbra or penumbra. The method is outlined in Vallado [47], and given in Equation set (2.34).

$$\begin{aligned} IF: \quad & \left[|\vec{r}_{sat}|sin(\phi)\right] \leq \left[tan(\alpha_{penumbra})\left(\frac{r_{\odot}}{\sin(\alpha_{penumbra})} + |\vec{r}_{sat}|\cos(\phi)\right)\right] \\ & SHADOW = PENUMBRA \\ IF: \quad & \left[|\vec{r}_{sat}|\sin(\phi)\right] \leq \left[\tan(\alpha_{umbra})\left(\frac{r_{\odot}}{\sin(\alpha_{umbra})} - |\vec{r}_{sat}|\cos(\phi)\right)\right] \\ & SHADOW = UMBRA \end{aligned} \tag{2.34}$$

SRP force modeling

Now that the vector from which incoming photons are coming from is established, and it is known when and how the stream of photons is cut from the spacecraft due to Earth shadowing, the force model for SRP can be introduced. First, the energy coming from the sun must be quantified. Baker provides the average solar flux as $1367 W/m^2$ [48], based on the number of photons reaching the Earth at a certain frequency and with a specific amount of energy. Using Einstein's famous energy mass relation [49], which eventually took the form $E = mc^2$, the solar pressure over some area at the average orbital distance of Earth can be calculated as in Equation set (2.35).

$$\begin{aligned} mc &= \frac{E}{c} \\ p_{SRP} &= \frac{1367}{3 * 10^8} \frac{[W/m^2]}{[m/s]} = 4.57 * 10^{-6} \frac{[N]}{[m^2]} \end{aligned} \tag{2.35}$$

Note that this calculation uses the average solar flux value. Higher fidelity analyses may consider using a variable solar flux value based on solar cycle information. By introducing a coefficient of reflectivity, C_R, an expression for the force on a spacecraft surface element due to SRP can be found. As in Vallado, [47], the coefficient can be taken to be between 0 and 2, with 0 meaning a transparent spacecraft that does not interact with incoming photons, 1 being a blackbody that absorbs all incoming photons, and 2 being a perfectly reflecting body. Similar to Equation set (2.30), the force, acceleration, and moment from SRP can be found as in Equation set (2.36).

$$\vec{F_{SRP}} = p_{SRP} C_R \sum A_i \hat{r}_{\odot - i}$$

$$\vec{a_{SRP}} = F_{SRP}/m \tag{2.36}$$

$$\vec{M_{SRP}} = p_{SRP} C_R \sum r_{cm,i} \times (A_i \hat{r}_{\odot - i})$$

Again, care must be taken as to what frames are being used. The acceleration again should be in ECI, whereas the torques should be in the body frame. Reference Section 2.1 for frame conversion information.

2.4.3 Gravitational perturbations

The final set of perturbations considered in this work are gravity based. The analyses of the two effects, Earth oblateness perturbations and gravity gradient torques, are separate. Earth oblateness analysis is concerned with quantifying the effect of an uneven mass distribution in the Earth, whereas gravity gradient torques are a result of uneven mass distributions in a spacecraft. For the Earth, spherical harmonics, in the form of zonal, sectoral, and tessoral harmonics are used to quantify the unevenness of Earth's mass distribution, and the resulting altered gravity field. For the spacecraft, the inertia tensor conveniently holds the information required to understand the mass distribution.

Earth Oblateness

Derivation of the non-spherical potential function that models the Earth's gravity field has been done in many forms, for example in Lambeck [50]. Here, the goal is to use a simplified model to obtain accelerations on the orbiting spacecraft that perturb the orbit. Most of the effects of oblateness can be captured simply by accounting for the second zonal term, often denoted J_2, and ignoring higher order terms J_n.

The end result of the accelerations derived from this analysis is usually that the orbit plane is rotated in the opposite direction of the motion of the spacecraft, while the argument of perigee increases [51]. Vallado [47] provides simple formulations for the accelerations on a spacecraft due to Earth oblateness. Higher order terms can be found in Escobal [52], but are omitted here since the extra computation gives diminishing returns on solution accuracy due to the small magnitude of the other J_n terms. The formulation for the J_2 accelerations is given in Equation set (2.37). The subscripts $_{x,y}$, and $_z$ represent the position of the spacecraft in ECI coordinates.

$$
\begin{aligned}
a_x &= -\frac{3J_2\mu_\oplus R_\oplus^2 r_x}{2r^5}\left(1-\frac{5r_z^2}{r^2}\right) \\
a_y &= -\frac{3J_2\mu_\oplus R_\oplus^2 r_y}{2r^5}\left(1-\frac{5r_z^2}{r^2}\right) \\
a_z &= -\frac{3J_2\mu_\oplus R_\oplus^2 r_z}{2r^5}\left(3-\frac{5r_z^2}{r^2}\right)
\end{aligned}
\tag{2.37}
$$

The z term here is perpendicular to the equator, extending through the north pole, whereas the x and y terms are in the equatorial plane, following ECI convention. These accelerations are already in the ECI frame, and can be used directly as a vector in Equation (2.6).

Gravity gradient torque

For most spacecraft, there exists a physical distance between the center of gravity and the center of mass. When the vectors between the center of mass and center of gravity are not aligned with the gravity vector, there exists a torque that acts to restore the orientation to such an aligned attitude. The magnitude of this torque is dependent on both the distribution of mass of the satellite, as well as the relative orientation to the gravity vector. A typical derivation exists in Wie [24], which uses direction cosines for orientation. In this work, the satellite coordinates are converted

to the body frame, and the resulting expressions for the torque due to gravity gradients are given in Equation set (2.38), with the subscripts $_x$,$_y$, and $_z$ again representing the position of the spacecraft in ECI coordinates.

$$\begin{aligned} M_x &= \frac{3\mu_\oplus}{r^5} r_y r_z (I_{33} - I_{22}) \\ M_y &= \frac{3\mu_\oplus}{r^5} r_x r_z (I_{11} - I_{33}) \\ M_z &= \frac{3\mu_\oplus}{r^5} r_x r_y (I_{22} - I_{11}) \end{aligned} \tag{2.38}$$

2.5 Numerical method

The propagator itself is written in MATLAB, which is efficient for vector operations and provides ample built in features for numerical simulation. A users guide of the propagation software is provided in the appendix. Here, a discussion on the methods used for numerical simulation will be discussed.

There are two operating modes of the simulation software, orbital mode and wind tunnel mode. Orbital mode is the 6DOF propagator that has so far been the topic of discussion, while wind tunnel mode is a 3DOF simulation that ignores trajectory, and only propagates attitude dynamics. While orbital mode is designed to recreate the dynamics of a spacecraft in orbit, wind tunnel mode is more of an analysis tool that can be used to gain a better understanding of the dynamic behavior of a spacecraft due to aerodynamic torques.

A large difference in the methods of propagation between the wind tunnel and orbital modes exists in the stiffness of the problems. The orbital mode must propagate both trajectory and attitude together, which effect the motion of the spacecraft on different time scales. While stiffness is not rigorously defined, a problem with multiple answer components that vary on different time scales can be thought of as stiff. Meanwhile, stiffness is not a relevant concern for the wind tunnel simulation.

MATLAB has several built-in differential equation solvers which are optimized for different types of problems, as described in Shampine [53]. While solvers such as

ode15s are designed to better handle stiff problems, they suffer from lower accuracy than newer nonstiff solvers such as ode113. For this work, it was seen that ode113 outperforms ode15s even for the stiff orbital case, and so ode113 is used for both the orbital and wind tunnel modes.

2.6 DSMC

To verify the accuracy of the aerodynamics formulation and determine the validity of the free molecular assumption for specific flow cases, the high fidelity DSMC method can be used. DSMC, first formulated by Bird in the 1960s [40], is a stochastic method that can model the molecular motion of particles in a flow by solving the Boltzmann equation. At a very simple level, the technique works by repeatedly moving and colliding simulated flow particles according to specified physical models and probabilities [54]. Due to the vast number of particles inherent in the simulated flows, the computational demand is high, even when simulated particles are used to account for over many trillions of real particles. The operation is still intensive, and to date around a dozen codes have been developed. In 2014, Sandia National Labs released an open source DSMC code, SPARTA (Stochastic PArallel Rarefied-gas Time-accurate Analyzer), which is a high speed code capable of efficient DSMC analysis [55] using parallel computing. SPARTA has been validated against test data [56], and the code enjoys excellent documentation and modularity [57], and has therefore been used in this work to analyze the aerodynamics of each tested geometry in a high fidelity environment.

2.7 Additional considerations

In modeling the solar radiation pressure and aerodynamics using free molecular flow, considerations on self shadowing become relevant. The current model used in the propagator is a simple shadowing model that determines if a surface element would be 'wetted' by incoming flow or radiation, but does not take into account self

shadowing from geometry upstream. This is typically a very computationally intensive calculation, especially for more complex spacecraft geometries with more surface elements. The simple model has been utilized in this work, but recommendations are made for exploring more complex models in the Future Work section.

A point of debate in this work is the dynamic modeling of the spacecraft motion in the atmosphere by accounting for aerodynamic damping factors. Work has been done for this topic in hypersonics using the Newtonian approach [58], which has been re-purposed for use in free molecular regimes [22]. There is not conclusive proof that this method of modeling aerodynamic damping is valid for free molecular regimes, so it has not been used in this work.

3. APPLICATION - LIGHTSAIL

As a whole, the Lightsail program is working towards progressing the current state of the art for solar sailing technologies. The first mission in the program, Lightsail 1, successfully demonstrated solar sail deployment on a 3U CubeSat in LEO in 2015 [59]. Lightsail 1 is an excellent example of the type of high area to mass ratio craft that could benefit from 6DOF analysis. Since the craft has already flown, it can be used as a validation case to test the 6DOF code's predictive ability.

3.1 Mission description and Modeling considerations

Lightsail 1 launched as a secondary payload aboard a United Launch Alliance Atlas V rocket on May 20th, 2015 into a 356 km x 705 km elliptical orbit with an inclination of 55 degrees. The craft was deployed two hours after launch, and recovered from several anomalies in flight before sail deployment on June 7th. After an image was returned confirming deployment, the mission was considered a success, and Lightsail 1 eventually deorbited seven days after deploying the sail, on June 14th.

Due to the large reflective solar sail and low orbit, Lightsail 1 was particularly suspect to aerodynamic and solar radiation pressure based perturbations. In order to test the model using Lightsail 1, the geometry must first be put into an STL file format. The spacecraft used a 3U CubeSat spacedart configuration, with the solar sail at the front. The geometry is shown in 3.1, with the point $[0, 0, 0]$ coinciding with the spacecraft center of mass.

In order to model Lightsail 1 in the six DOF simulation, the physical parameters of the spacecraft and the initial state must be identified. These values are shown in Table 3.1.

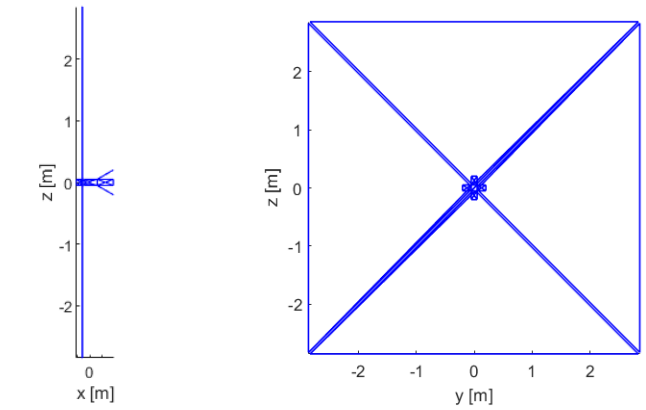

(a) Side view (b) Front view

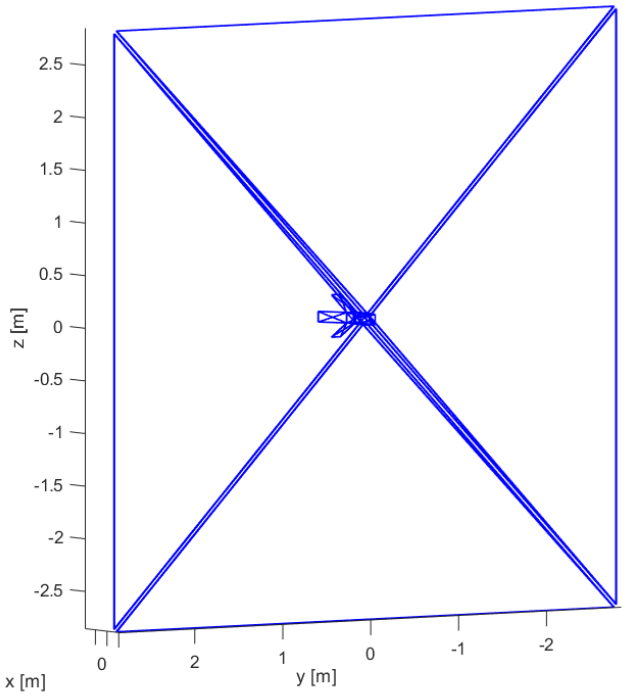

(c) Isometric view

Fig. 3.1. Lightsail geometry represented in STL format

The spacecraft mass and inertia properties are directly from Lightsail 1 technical documentation. The surface reflectance coefficient is an assumption that approximates the total surface of the spacecraft to be 90 percent reflective, and the surface is

Table 3.1.
Lightsail 1 6DOF simulation initial conditions and parameters

Parameter	**Value**
Inertia matrix $[kg * m^2]$	$\begin{bmatrix} 7.33 & 0 & 0 \\ 0 & 3.79 & 0 \\ 0 & 0 & 3.79 \end{bmatrix}$
Mass $[kg]$	4.93
Surface reflectance coefficient	1.8
Surface temperature $[K]$	350
Semi-major axis $[km]$	6908
Eccentricity	.0253
Inclination $[deg]$	55
Argument of perigee $[deg]$	0
Right ascension $[deg]$	0
Initial roll angle $[deg]$	0
Initial pitch angle $[deg]$	70
Initial yaw angle $[deg]$	50
Initial roll rate $[deg/s]$	14
Initial pitch rate $[deg/s]$	-5
Initial yaw rate $[deg/s]$	-1
Epoch [dd-mm-yyyy HH:MM:SS]	07-06-2015 12:00:00

assumed to be at an average of 350K. The surface temperature can certainly change over time, which can effect how particles interact with the surface, but the energy flux to the spacecraft is not modeled in this simulation. The initial orbital state used is based on the launch vehicle insertion, and the initial attitude state is provided by telemetry packets downlinked from the spacecraft for the time at deployment. Since the telemetry packets came at a delay, there is no attitude telemetry that is available

for the time directly after deployment. Instead, to account for some uncertainty in the rotational state after sail deployment, the packets directly prior to deployment, and the first set of packets available after sail deployment were averaged to determine an approximate initial post-deployment rotational state. Using this information, the 6DOF simulation was initialized and ran until the deorbit of the lightsail craft, which the simulation detects when altitude is below 150 km. The actual spacecraft deorbited on June 14th 2015, seven days after sail deployment, and the goal of this validation is to see how accurately this deorbit time can be reproduced using only the geometry of the spacecraft and initial conditions described in Table 3.1.

3.2 6DOF simulation results

The simulation provides insight on both the overall attitude and trajectory behavior of the spacecraft, as well as the individual contributors of the torques and forces from gravity, solar radiation pressure, and aerodynamics. First, the overall deorbit timeline can be assessed using the plot of altitude history, shown in Figure 3.2.

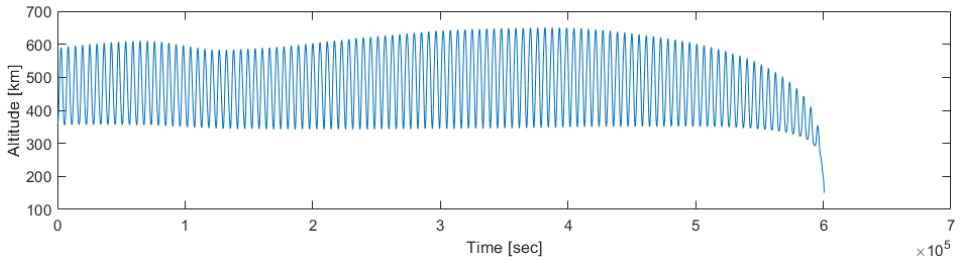

Fig. 3.2. Lightsail 1 simulated altitude history

The plot demonstrates that the software simulated about 600600 seconds of flight time, after which it detected that the craft deorbited (deorbit is detected when altitude dips below 150 km), and thus ended the simulation. This time corresponds to 6.95 days of flight time, which closely matches the true flight lifetime of the spacecraft after the sail was deployed. Spacecraft telemetry from the majority of the Lightsail

1 deorbit phase is unavailable due to a telecom anomaly during flight, and so the attitude state history cannot directly be confirmed. Still, the successful prediction of the overall deorbit time of the spacecraft is a good indication as to the accuracy of the simulation. To gain further insight on the spacecraft state history, specific histories of the gravitional, solar radiation pressure, and aerodynamics based perturbations are analyzed.

First consider the gravitational perturbations, shown in Figure 3.3. The gravity gradient torque is expected to orient the center of gravity between the attracting body and the spacecraft center of mass, and is a destabilizing torque when considering the dominant effect of aerodynamics in LEO. The non-spherical gravity potential will effect the trajectory based on the position of the craft over the Earth, and works to precess the orbit plane.

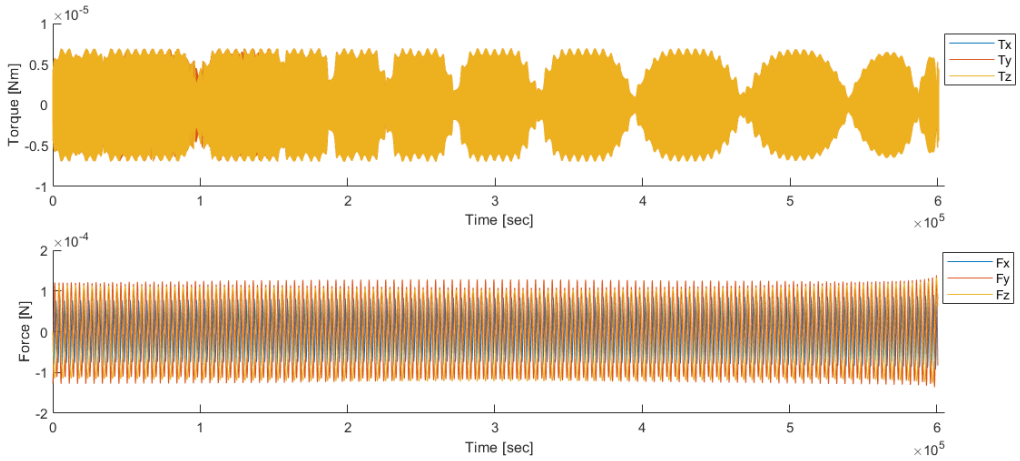

Fig. 3.3. Lightsail 1 simulated gravitational perturbation history

The precession of the orbit plane is apparent when looking at the 3D orbit geometry, shown in Figure 3.4.

The gravity gradient torque, like all the other perturbing torques, is a function of the environment and the relative spacecraft orientation. The orientation relative to the orbital velocity vector in the NTW frame can be used to determine aberration

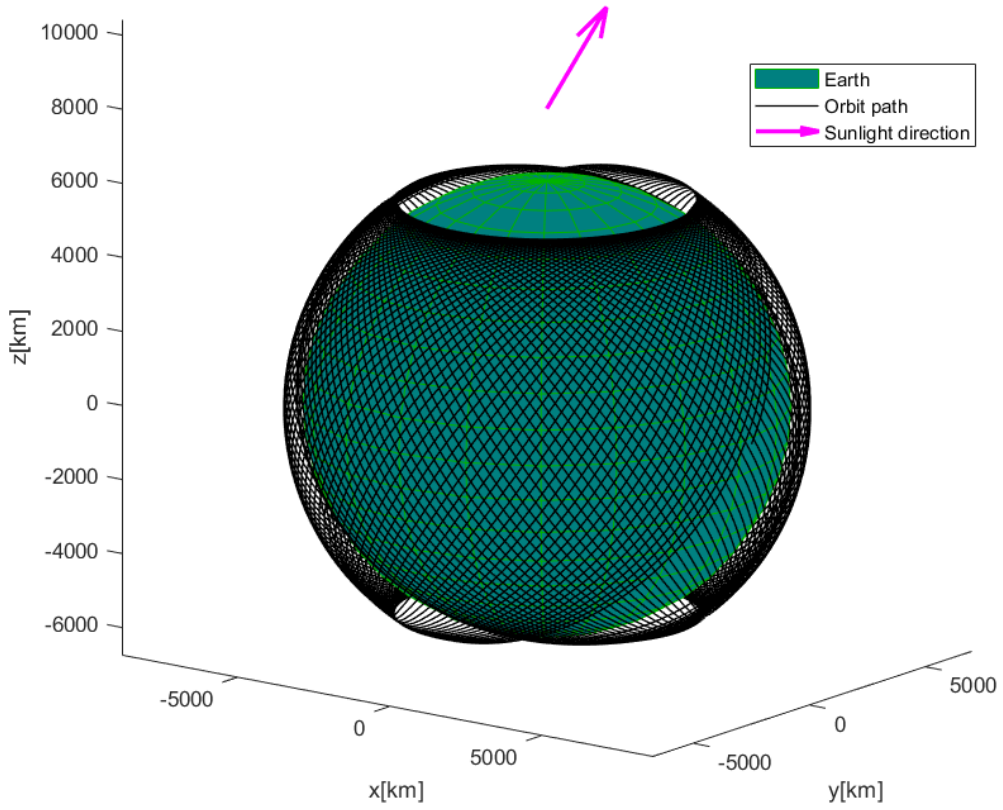

Fig. 3.4. Lightsail 1 simulated orbital motion history

from the trimmed orientation. A total orientation offset, or total angle of attack, can be determined from the combined magnitude of the yaw and pitch angles, shown in Figure 3.5. This figure shows an interesting trend for the geometry to tend towards orienting itself backwards relative to the flow, with the sail downstream of the CubeSat body, rather than having the sail upstream of the body as shwon in Figure 3.1. The reason for this is the offset between the center of pressure and center of mass.

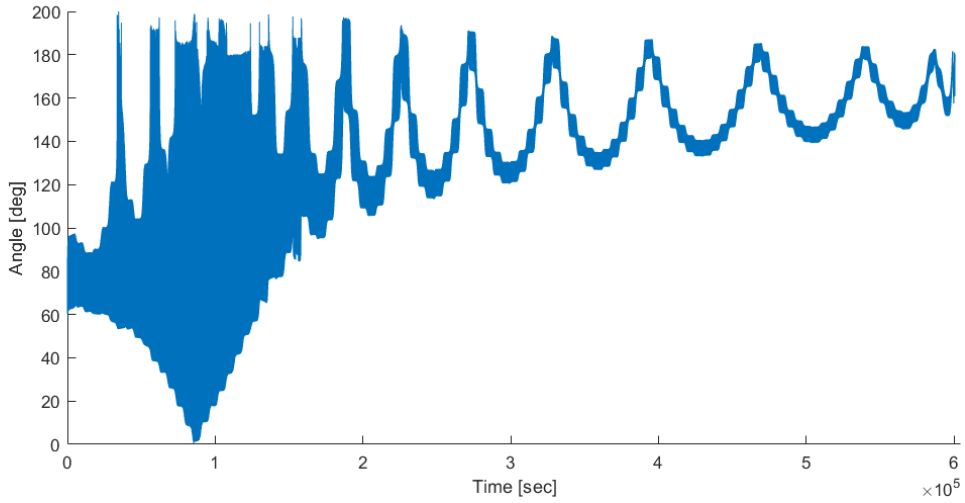

Fig. 3.5. Lightsail 1 simulated combined total angular displacement from flow velocity vector based on yaw and pitch

In Figure 3.1, the displacement between the main sail, which is approximately where the center of pressure lies in the nominal state, and the center of mass, is apparent. The initial orientation in this figure, with the center of pressure upstream of the center of mass, is inherently unstable, and leads to the seemingly chaotic rotational motion near the beginning of the simulation. After some time, the aerodynamic restoring torques are given time to adjust the spacecraft towards the passively stable orientation, which happens to be backwards, with the CubeSat body upstream of the sail. This trimming effect brings the craft to its maximum drag orientation, which then explains why the deorbit near the end of the simulated mission seems so sudden - instead of tumbling, the spacecraft is passively being oriented in the maximum drag orientation. The aerodynamic forces and torques can be seen in Figure 3.6.

In the aerodynamics figure, it is clear where the perigee and apogee passes occur due to the respective spike and drop in aerodynamic perturbing effects on the spacecraft. Of interest is also the large increase in aerodynamic force near the end of the mission, which is the direct cause of deorbit, as seen at the end of the altitude plot.

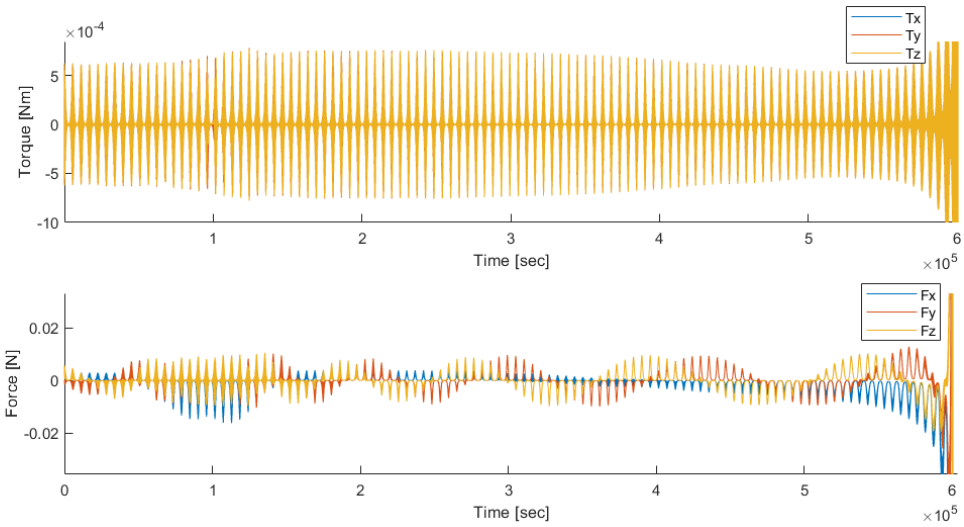

Fig. 3.6. Lightsail 1 simulated aerodynamic forces and torques

Finally, to account for the apogee raise near the middle of the mission as shown in the altitude plot, the solar radiation pressure effects plot can be examined, as shown in Figure 3.7. From this figure, it can be seen that there is an interesting combination of the sun position vector and orbit geometry that leads to an extended period in which the satellite does not pass behind the Earth, leading to an increase in the net effect of SRP. Unlike the aerodynamics plot where the drop off in force signifies a return to apogee, the SRP is dependent on the satellite position relative to the Earth's umbra and penumbra. These shadow positions are constant through the simulation, but there is nothing that dictates the spacecraft must pass through a shadow every orbit. The precession of the orbit by the Earth's non-spherical gravity potential leads the spacecraft to approach an orbit that exposes it to extended sunlight, which subsequently effects the overall trajectory significantly, as reflected in the altitude plot.

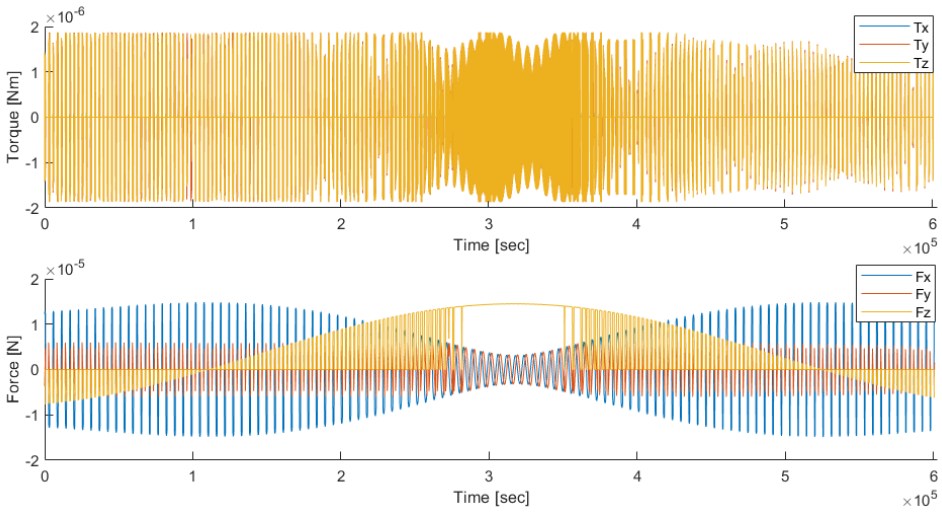

Fig. 3.7. Lightsail 1 simulated solar radiation pressure forces and torques

3.3 DSMC comparison

Using the Direct Simulation Monte Carlo method, the magnitude of the force on the body exerted by the particles in the flow can be determined. Comparing this to the force magnitudes determined by the simulation can give insight on the accuracy of the simulation. For the Lightsail 1 spacecraft, the geometry used in the DSMC runs is the same as shown in Figure 3.1. The parameters used in the DSMC calculation using SPARTA can be found in Appendix B, outlining the specific run inputs like number density, species composition, grid size, and other parameters. For this comparison, the spacecraft was oriented at four different angles of attack, each separated by 30 degrees. A demonstration of the pitch rotation for a 30 degree angle of attack is shown in Figure 3.8. The results for the calculations are shown in Table 3.2.

An interesting observation is that the simulation estimates a higher force for the non perturbed orientation, but then the DSMC estimates a higher force for the perturbed orientations. Once again looking at the lightsail geometry, it seems that the large sail at the front of the craft would shadow the back of the craft from any par-

ticle interactions. This shadowing is automatically taken into account using DSMC, but the free molecular code in the simulation does not have a shadowing formulation complex enough to take this into account. The result is that there is a slight overestimation in the force for the back of the spacecraft. For the perturbed orientations, the concave nature of the body can be used to describe the force discrepancy. The free molecular approximation is suited for convex bodies, since there is nothing used in the formulation to account for self-reflected particles, meaning particles that strike one surface of the craft and then bounce off to impart more momentum on another surface. Here, this explanation can be used to describe why the greater pertubations have in fact a greater force magnitude for the DSMC runs.

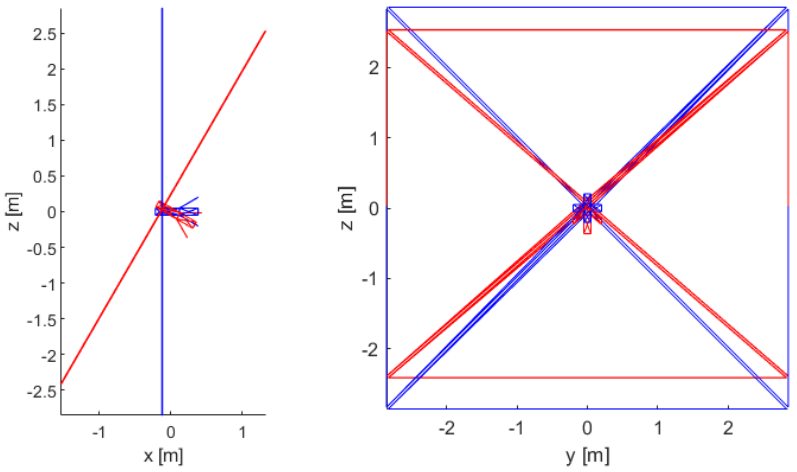

(a) Side view (b) Front view (freestream projection)

Fig. 3.8. Lightsail geometry (blue) and Lightsail geometry pitched by 30 degrees (red)

Overall, the difference is subtle, and the DSMC shows that the free molecular approximation used for this modeling can give reasonable results.

Table 3.2.
Lightsail 1 DSMC aerodynamics comparison

Angle of attack [deg]	**Force DSMC [N]**	**Force 6DOF [N]**	**% Difference**
0	0.009012	0.009072	0.66
30	0.007758	0.007105	8.42
60	0.004394	0.003978	9.47
90	0.000605	0.000234	61.32

3.4 Conclusions

Although there is a demonstrated discrepancy between the 6DOF simulation aerodynamic results and the SPARTA DSMC results, the simulated deorbit timeline closely matches the true deorbit time of the Lightsail 1 spacecraft. An important factor to consider here is the significance of the rotational initial conditions on the final result. Here, initial conditions for the simulation were provided through telemetry data from actual flight downlink packets, but in predictive cases, this information is unavailable. For proper prediction of the orbit profiles of missions that have yet to fly, a Monte Carlo use of the 6DOF simulation, where multiple initial angular rates and states are used, could potentially give the best insight. Further, it cannot be said with certainty that the simulation is highly accurate because of this prediction. Certain spacecraft geometries may more readily expose the shortcomings of the free molecular aerodynamic approximation, and could be susceptible to effects like structural deformation or changes in mass properties during orbit, neither of which are currently in the simulation's capability to predict.

4. APPLICATION - SAIL-BOOM-ROCKET

Much of the space debris in orbit around Earth can be traced back to to the spent upper stages of launch vehicles. These objects are large and can pose a significant collision risk to other objects in orbit. One of the concepts being considered to safely deorbit these objects is a craft that can rendezvous with the debris, attach to it, and deploy a drag sail on a boom. The boom acts to offset the center of pressure from the center of mass, providing a restoring torque that will passively help the structure maintain the maximum projected area to the flow for the fastest possible deorbit. The geometry used here is shown in Figure 4.1.

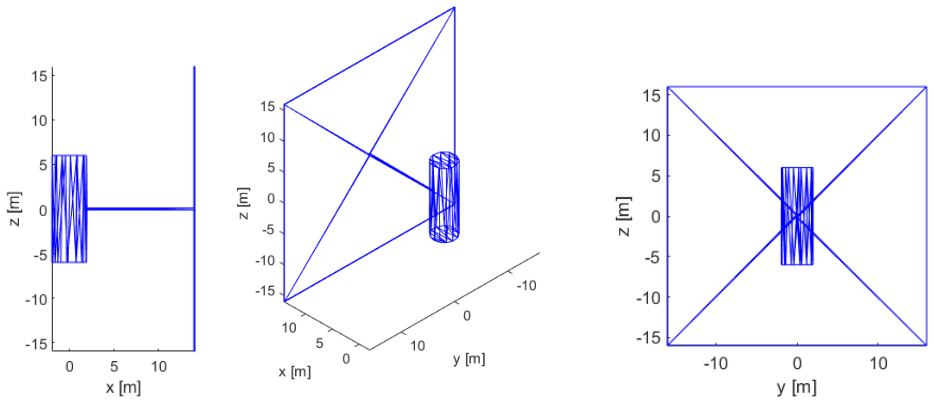

(a) Side view (b) Isometric view (c) Front view

Fig. 4.1. SBR geometry represented in STL format

4.1 Mission description and Modeling considerations

Although there has been no mission to date demonstrating this technology, a hypothetical scenario can be analyzed using the 6DOF simulation. Of particular

interest is the attitude behavior over time and ability to damp a perturbation through aerodynamic restoring torques at varying altitudes.

Consider the set of initial conditions in Table 4.1 for analysis with the 6DOF simulation. Inertia and mass properties describe a representative rocket body geometry, with the surface reflectance estimated based on the combination of a slightly reflective body and transparent sail.

Table 4.1.
SBR 6DOF simulation initial conditions and parameters

Parameter	**Value**
Inertia matrix $[kg * m^2]$	$\begin{bmatrix} 16600 & 0 & 0 \\ 0 & 107900 & 0 \\ 0 & 0 & 107900 \end{bmatrix}$
Mass $[kg]$	8329.942
Surface reflectance coefficient	.5
Surface temperature $[K]$	350
Semi-major axis $[km]$	7028.1, 6878.1, 6828.1
Eccentricity	0
Inclination $[deg]$	0
Argument of perigee $[deg]$	0
Right ascension $[deg]$	0
Initial roll angle $[deg]$	0
Initial pitch angle $[deg]$	20
Initial yaw angle $[deg]$	10
Initial roll rate $[deg/s]$	0
Initial pitch rate $[deg/s]$	0
Initial yaw rate $[deg/s]$	0
Epoch [dd-mm-yyyy HH:MM:SS]	10-05-2020 12:00:00

4.2 6DOF simulation results

Three different orbital altitudes are considered, with each case propagated for one day. The total longitudinal angle offset for the 650 km orbit case is shown in Figure 4.2. In this figure, there is no apparent damping to the maximum drag attitude over the time shown, and instead the spacecraft is seen to be tumbling.

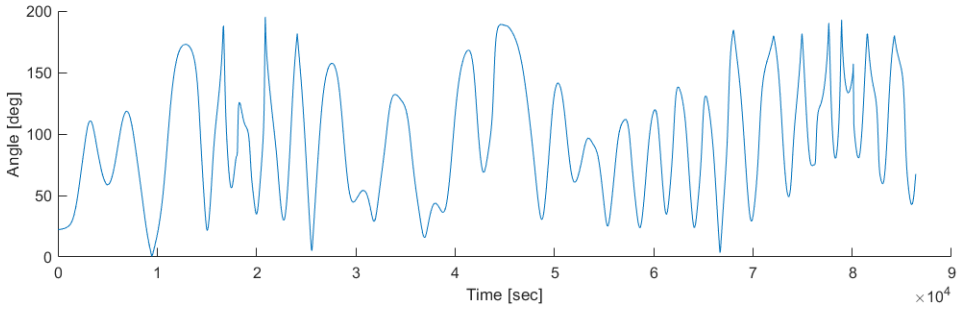

Fig. 4.2. SBR simulated combined total angular displacement from flow velocity vector based on yaw and pitch, 650 km case

To analyze the cause of this, the magnitudes of the different perturbation sources are examined. First, consider the aerodynamic perturbation, with the force and torque component histories shown in Figure 4.3. It is seen that the total magnitude for the torque is never greater than 0.2 Nm, and the maximum torque experienced for the time is 0.1806 Nm.

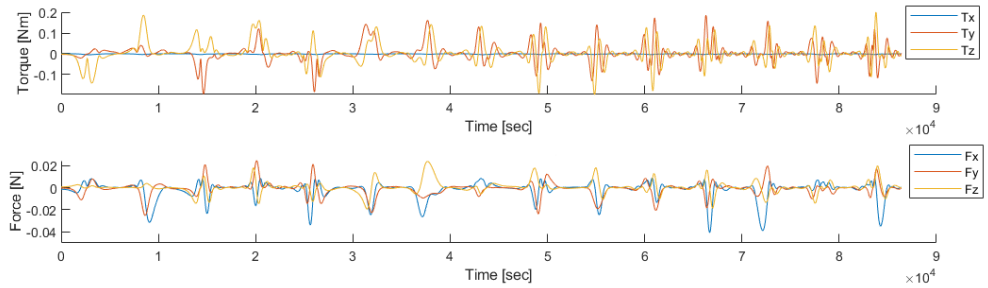

Fig. 4.3. SBR simulated aerodynamic perturbation history, 650 km case

Next, consider the gravity based perturbations, shown in Figure 4.4. The torques here are on the same order of magnitude as the aerodynamic torques in the previous figure, with the maximum torque being 0.1630 Nm.

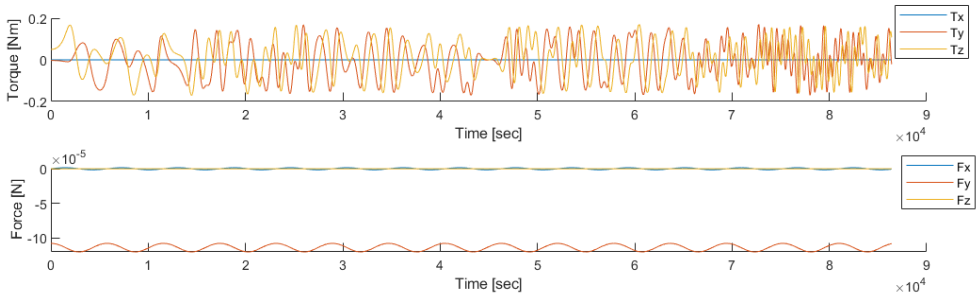

Fig. 4.4. SBR simulated gravitational perturbation history, 650 km case

Finally, the solar radiation pressure based perturbations can be examined, shown in Figure 4.5.

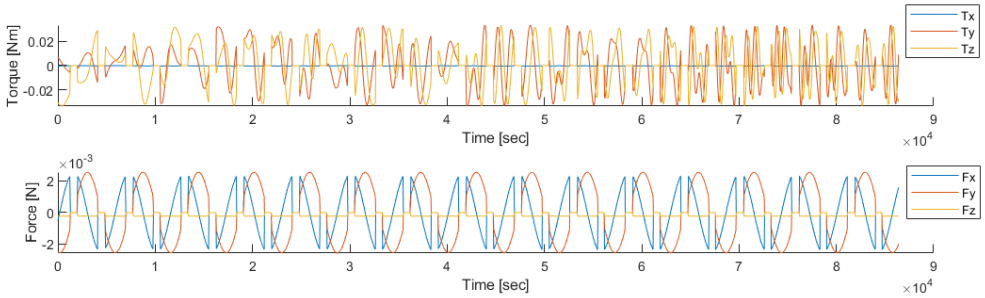

Fig. 4.5. SBR simulated solar radiation pressure perturbation history, 650 km case

In summary, for the 650km case, the aerodynamic torques are not yet sufficient to stabilize the spacecraft into the maximum drag orientation.

Next, the 500 km orbit case can be considered. Here, it is expected that the effect of aerodynamics is greater, and so a more stabilized behavior may be expected. The total combined angular displacement for the 500 km case is shown in Figure 4.6, where there is clearly more of a trend for the spacecraft to trim to the maximum drag orientation.

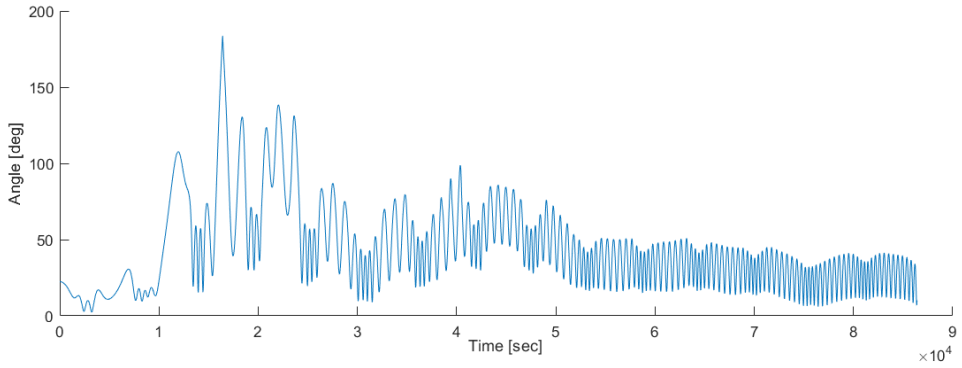

Fig. 4.6. SBR simulated combined total angular displacement from flow velocity vector based on yaw and pitch, 500 km case

Again, further insight can be gained from analysis of the individual perturbation sources. The aerodynamic force and torque components are shown in Figure 4.7. The aerodynamic torques in this case are nearly 25 times higher than those in the 650 km case, explaining why there is a trend to trim to the maximum drag orientation.

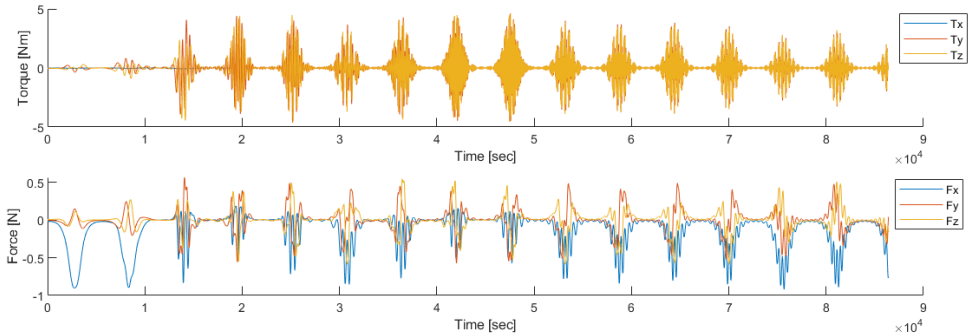

Fig. 4.7. SBR simulated aerodynamic perturbation history, 500 km case

The gravity based perturbations shown in Figure 4.8, while larger in magnitude than in the 650 km case, do not nearly approach the magnitude of the aerodynamic perturbing torques.

Similarly, the solar radiation pressure forces and torques, shown in 4.9, are essentially the same magnitude as those in the 650 km case.

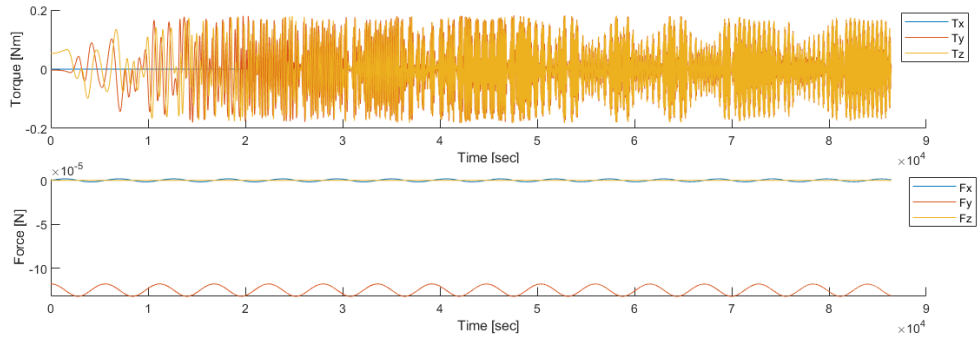

Fig. 4.8. SBR simulated gravitational perturbation history, 500 km case

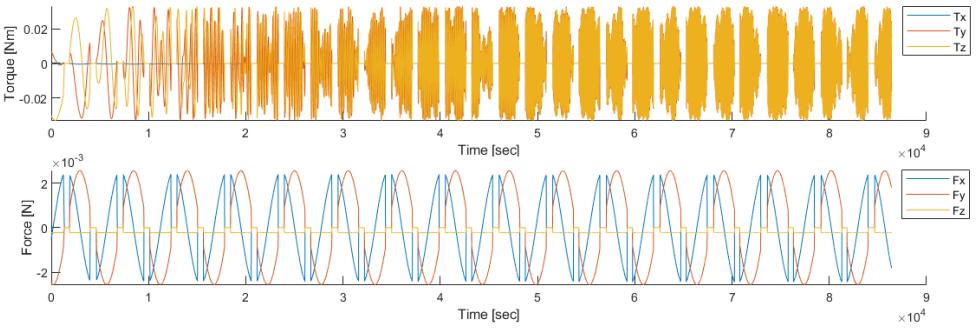

Fig. 4.9. SBR simulated solar radiation pressure perturbation history, 500 km case

Because the atmosphere increases in density so rapidly as altitude decreases, an orbit altitude difference of 150 km is sufficient to see the transition from tumbling motion to marginal stability. Finally, the 450 km case can be observed to further demonstrate this phenomenon. The total combined angular displacement plot is shown in Figure 4.10. Wheras the 500 km case ended up seemingly oscillating about a total angle of around 25 degrees, the 450 km tightens this oscillation around seven degrees. This is because the magnitude of the aerodynamic restoring torque has again increased. While the other perturbing effects are non-zero, their effects begin to diminish more and more with decreased altitude as the aerodynamic torque becomes more and more dominant.

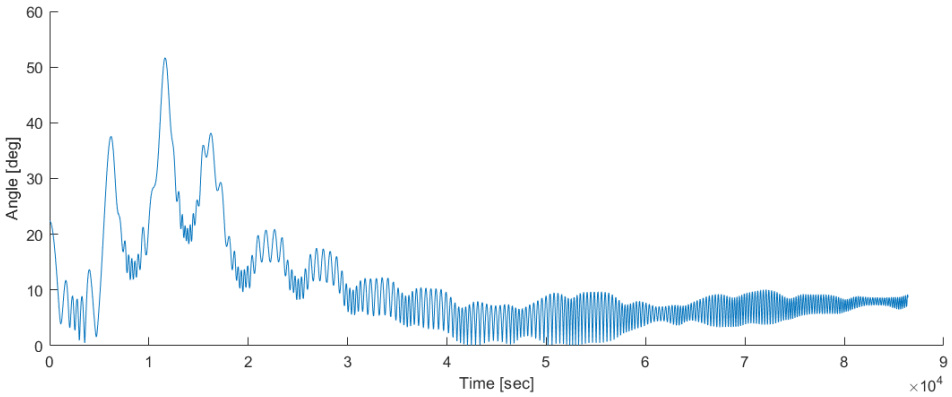

Fig. 4.10. SBR simulated combined total angular displacement from flow velocity vector based on yaw and pitch, 450 km case

The aerodynamic force and torque components for this 450 km case are shown in Figure 4.11, with the gravity based perturbations shown in Figure 4.12, and the solar radiation pressure perturbations shown in 4.13

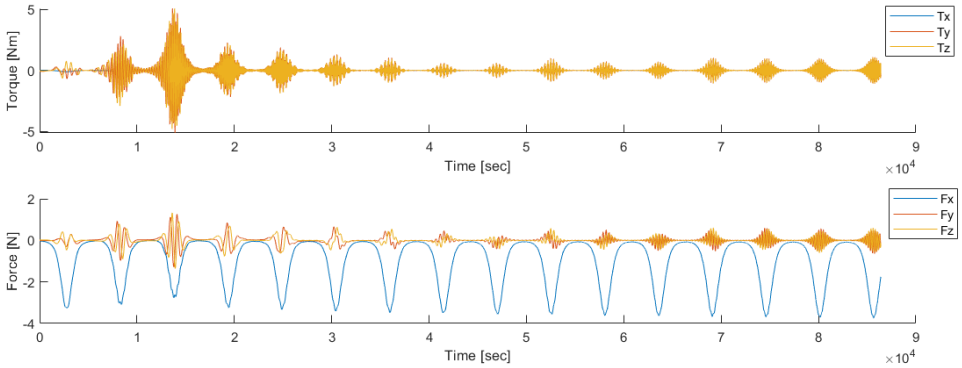

Fig. 4.11. SBR simulated aerodynamic perturbation history, 450 km case

Overall, it is seen that at a 650 km altitude, the aerodynamic, gravitational, and solar radiation pressure torques are around the same magnitude, but the aerodynamic perturbations quickly take over as the dominant effect as altitude decreases. This geometry has the ability to passively damp perturbations by virtue of the inherent

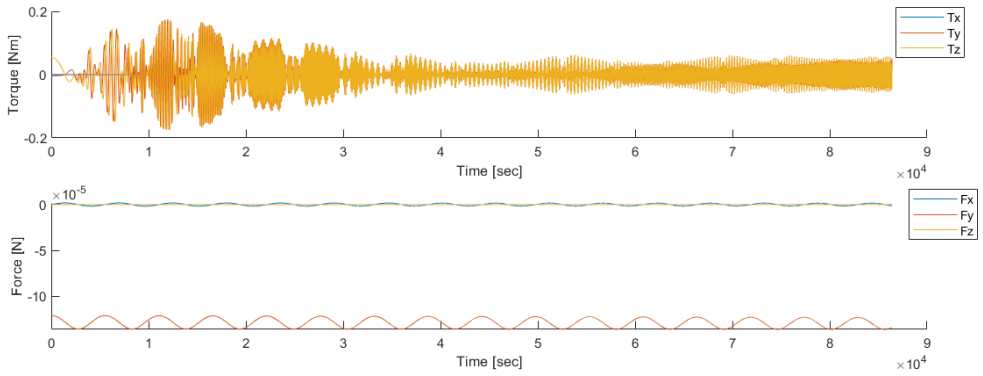

Fig. 4.12. SBR simulated gravitational perturbation history, 450 km case

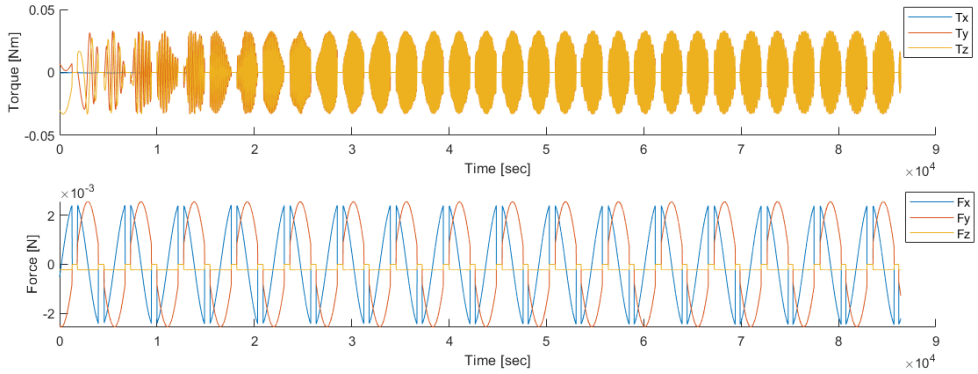

Fig. 4.13. SBR simulated solar radiation pressure perturbation history, 450 km case

offset between the center of pressure and center of mass in the nominal orientation, since the resulting restoring torque acts to trim the attitude.

4.2.1 DSMC comparison

Using the SPARTA DSMC code, the aerodynamic force magnitude on the SBR craft was calculated for the 650 km circular orbit case. The results are compiled in Table 4.2, with the parameters used to run the analysis contained in Appendix B.

Again, the results suggest that the lack of more accurate shadowing leads the free molecular approximation to slightly overestimate the force in the unperturbed

Table 4.2.
SBR DSMC aerodynamics comparison

Angle of attack [deg]	**Force DSMC [N]**	**Force 6DOF [N]**	**% Difference**
0	0.001485	0.001542	3.84
30	0.001275	0.001211	5.02
60	0.000767	0.000648	15.51
90	0.000163	0.000094	42.33

orientation. In the perturbed state, the concave geometry and subsequent surface reflections cause a larger force than the 6DOF simulation predicts, due to the fact that these re-emitted particles are not modeled. The simulation overall provides a fairly accurate approximation of the aerodynamic forces acting on the spacecraft in orbit.

4.3 Conclusions

This example demonstrated the feasibility of a physical offset boom to create a center of pressure/center of mass offset in order to induce restoring torques to trim a spacecraft to the maximum drag orientation for fast deorbit and debris mitigation. At higher altitudes, the aerodynamic torques are unable to overcome the gravitational and SRP torques that perturb the craft, and there is a tumbling motion. At lower altitudes however, the geometry serves its purpose and takes advantage of the aerodynamic restoring torques to maximize the frontal projected area. An interesting note is that while the gravity gradient torques and aerodynamic perturbation magnitudes varied as a function of altitude, the solar radiation pressure perturbations were mostly constant. For an uncontrolled spacecraft or object in a high orbit, this could lead to tumbling.

5. APPLICATION - AERODYNAMIC DEORBIT EXPERIMENT

The Aerodynamic Deorbit Experiment 1U CubeSat will provide flight qualification and characterize the performance of a deployable drag device to accelerate the deorbit of small satellites. ADE will test the passively stable pyramid sail technology developed by Long [22]. While a concept like the sail-boom-rocket device creates an offset between the center of pressure and center of mass through using a long boom, the passively stable pyramid sail instead angles back the drag sail itself, leading to a more compact design while still facilitating the use of aerodynamic restoring torques to maintain the maximum drag orientation.

5.1 Mission description and Modeling considerations

ADE will be deployed by a Poly-Picosatellite Orbital Deployer (PPOD) from a United Launch Alliance Atlas V as a secondary payload into a geosynchronous transfer orbit (GTO). Upon spacecraft checkout, ADE will deploy a drag sail, nominally during tracking coverage, and will begin the main phase of its mission as it slowly deorbits. The extremely elliptical orbit allows for small windows centered around perigee where significant aerodynamic drag perturbs motion. At these perigee passes, an on-board inertial measurement unit will quantify the acceleration and observe the spacecraft rotational rates to assist in characterizing the performance of the drag device. An illustration of the GTO trajectory is shown in Figure 5.1.

The ADE geometry is based on the work done by Long [22], and is represented here for simulation by the STL geometry shown in Figure 5.2.

The initial conditions for the simulation are provided in Table 5.1

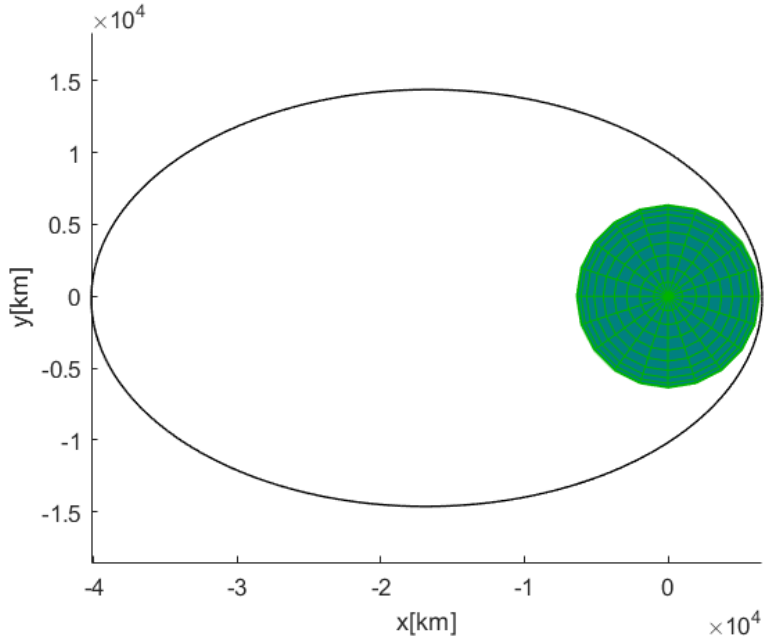

(a) GTO out of equatorial plane view

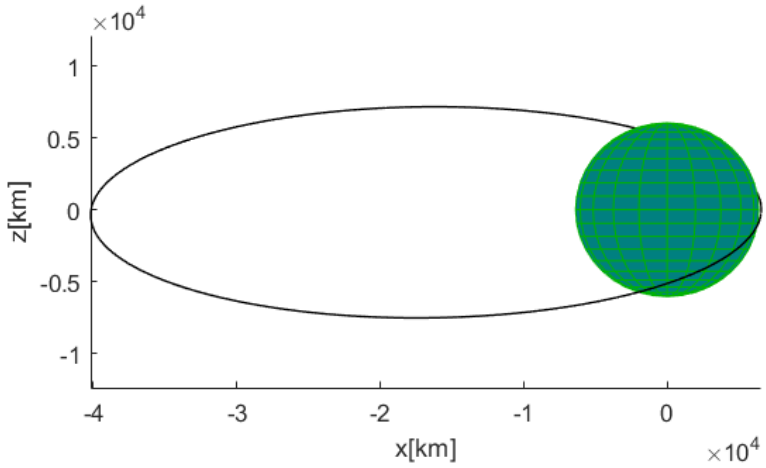

(b) GTO equatorial plane view

Fig. 5.1. Geosynchronous trasnsfer orbit geometry

As described, the initial orbit is modeled to be a geosynchronous transfer orbit. The initial conditions for the attitude are randomly selected as a predicted rotational

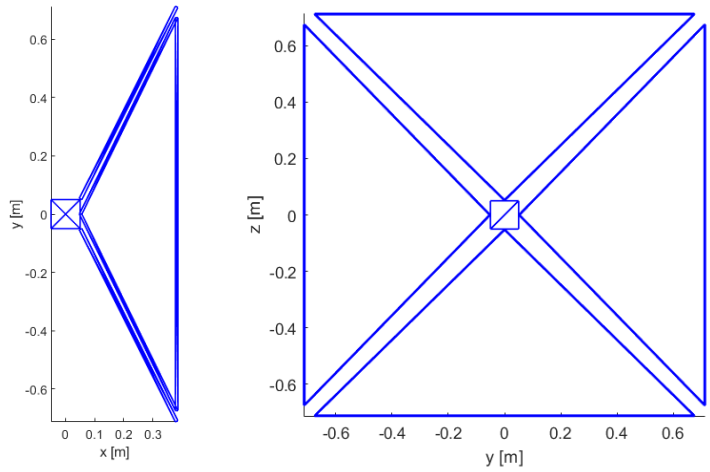

(a) ADE side view (b) ADE front view

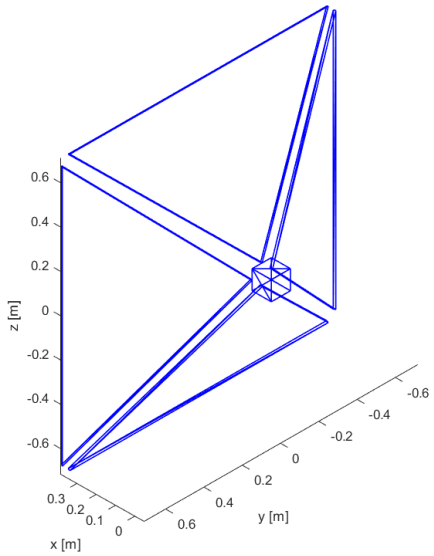

(c) ADE isometric view

Fig. 5.2. ADE geometry represented in STL format

state after sail deployment, and the epoch is an approximate time that launch may occur at, as ADE has yet to be confirmed for a specific flight. Since the sail material to be used, CP-1, is transparent, a very low reflectance coefficient has been selected. After sail deployment, ADE will gather and downlink accelerometer and gyro data

Table 5.1.
ADE 6DOF simulation initial conditions and parameters

Parameter	**Value**
Inertia matrix $[kg * m^2]$	$\begin{bmatrix} 0.075 & 0 & 0 \\ 0 & 0.05 & 0 \\ 0 & 0 & 0.05 \end{bmatrix}$
Mass $[kg]$	2.0
Surface reflectance coefficient	.01
Surface temperature $[K]$	350
Semi-major axis $[km]$	24348.2
Eccentricity	.73062
Inclination $[deg]$	27
Argument of perigee $[deg]$	0
Right ascension $[deg]$	0
Initial roll angle $[deg]$	15
Initial pitch angle $[deg]$	20
Initial yaw angle $[deg]$	10
Initial roll rate $[deg/s]$	-2
Initial pitch rate $[deg/s]$	3
Initial yaw rate $[deg/s]$	1
Epoch [dd-mm-yyyy HH:MM:SS]	07-06-2020 12:00:00

for at least five perigee passes. The spacecraft will frequently be flying through the Val Allen radiation belts, so a quick time line to achieve mission success after sail deployment is desirable. A 6DOF analysis has been performed on the first week of the ADE mission after sail deployment, to simulate what the behavior of the craft will be as it travels the initial highly elliptical orbit that will provide the data required for full mission success.

5.2 6DOF simulation results

From the initial epoch, a period of seven days has been examined for the Aerodynamic Deorbit Experiment. The Euler angle history is shown in 5.3. The altitude history is shown in 5.4 to reference where perigee passes occur. The angle histories indicate that the spacecraft is precessing and nutating about the longitudinal axis while spinning, with abrupt changes in behavior at every perigee pass. A green box is used to indicate a time period surrounding a sample perigee pass. A zoomed in view of this green area is provided in 5.5

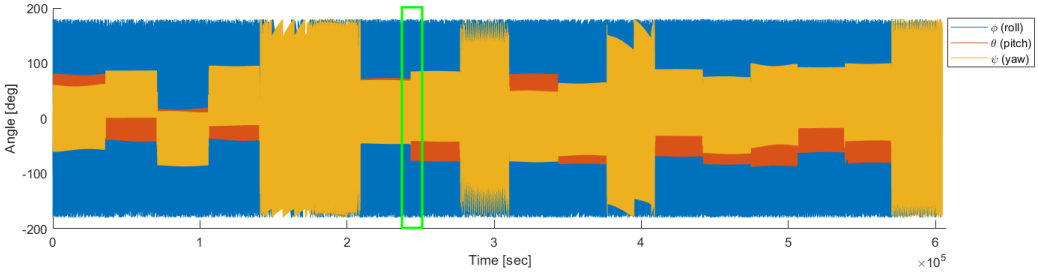

Fig. 5.3. ADE simulated Euler angle history for first seven days after sail deployment

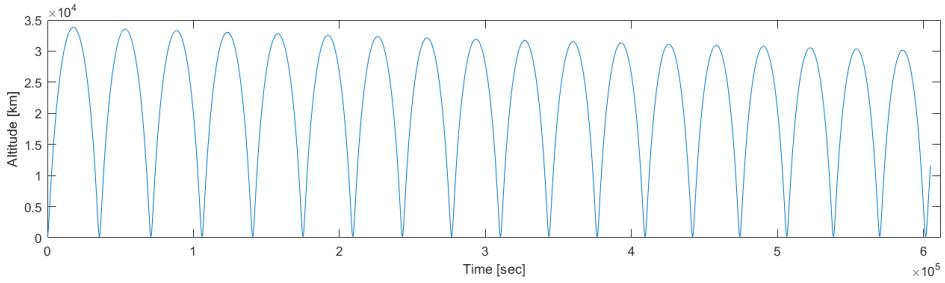

Fig. 5.4. ADE simulated orbital altitude history for first seven days after sail deployment

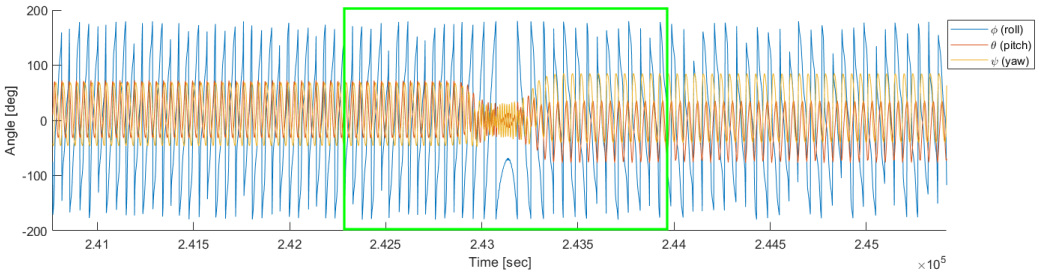

Fig. 5.5. ADE simulated Euler angle history for first seven days after sail deployment, zoomed in on a perigee pass

The zoomed in plot demonstrates that while ADE is in a loosely bound, marginally spin stabilized attitude induced by environmental torques at high altitudes, the craft tends to trim to the maximum drag orientation during perigee passes due to the restoring torques generated by the center of pressure center of mass offset. This stabilization at low altitudes is critical to the ADE mission, since the sail geometry used has been designed specifically to stabilize the craft in the presence of aerodynamic torques. With this stabilization, the craft oscillates within a 30 degree total angle of attack displacement during the perigee pass, providing more drag than would a tumbling state, and decreasing the orbital lifetime. The aerodynamic perturbation history shows how the aerodynamic effects spike at every perigee pass in Figure 5.6, with a zoomed in version shown in Figure 5.7.

As the spacecraft ascends in orbit following perigee, the aerodynamic effects rapidly diminish, and the angular rates imparted by the perigee pass are maintained in the orbit until the next perigee pass again perturbs the motion. In the altitude history plot, it can be seen that apogee decreases by nearly four thousand kilometers in the first seven days alone.

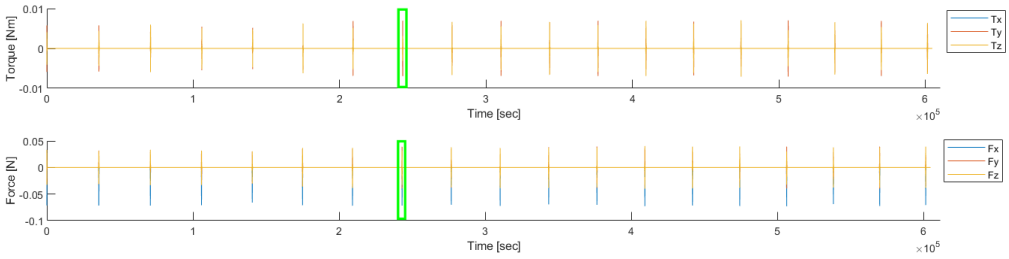

Fig. 5.6. ADE simulated aerodynamic perturbation history for first seven days after sail deployment

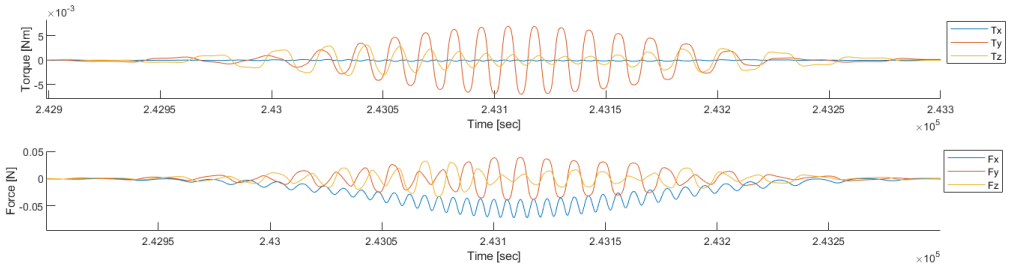

Fig. 5.7. ADE simulated aerodynamic perturbation history for first seven days after sail deployment, zoomed in on a perigee pass

The gravitational perturbations, shown in Figure 5.8 are the most intense near perigee, but never come close in magnitude to the aerodynamic perturbations. The effects of the J_2 perturbation are also made apparent when observing the 3D orbit geometry, shown in Figure 5.9. The solar radiation pressure perturbations, shown in Figure 5.10 act very weakly on the mostly transparent ADE spacecraft, but are nearly continuously applied due to the orbit geometry and sun position for this case.

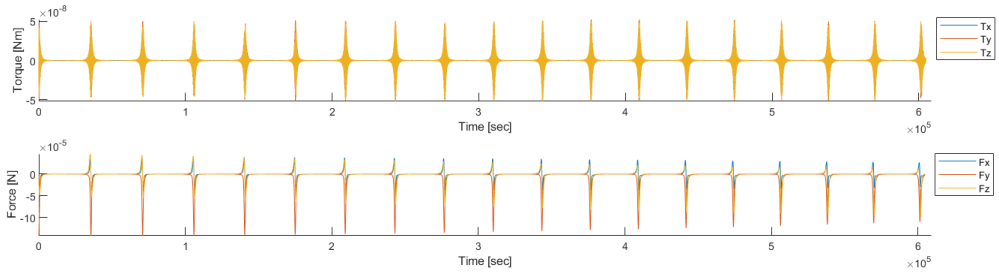

Fig. 5.8. ADE simulated gravitational perturbation history for first seven days after sail deployment

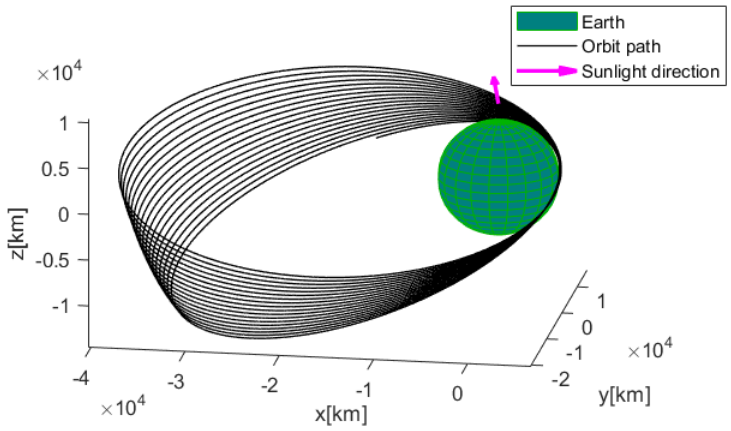

Fig. 5.9. ADE simulated trajectory for first seven days after sail deployment

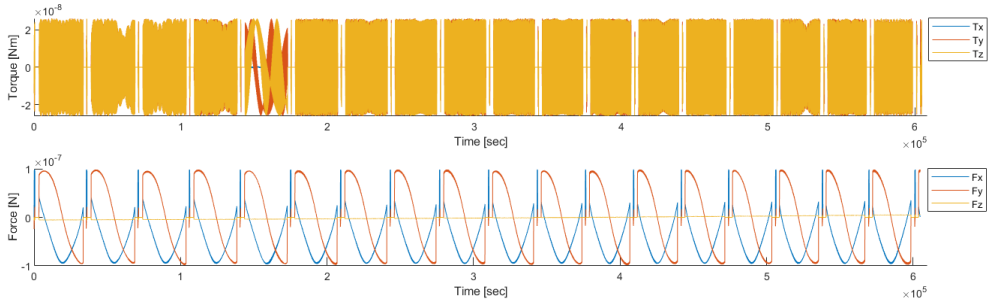

Fig. 5.10. ADE simulated solar radiation pressure perturbation history for first seven days after sail deployment

5.3 DSMC comparison

The ADE spacecraft was similarly analyzed using DSMC to compare to the aerodynamic formulation used in the 6DOF code. The results are shown in Table 5.2.

Table 5.2.
ADE DSMC aerodynamics comparison

Angle of attack [deg]	**Force DSMC [N]**	**Force 6DOF [N]**	**% Difference**
0	0.098503	0.094237	4.33
30	0.085155	0.072496	14.88
60	0.050519	0.035605	29.52
90	0.017727	0.004186	76.39

This comparison is an excellent example of the shortcomings of the simplified shadowing analysis. While the comparison shows good agreement in orientations where self shadowing is not an issue, it breaks down when geometry is placed upstream of other geometry. This phenomenon is captured in Figure 5.11. In this figure, it is clear that in the 90 degree angle of attack orientation, the sail segment upstream should be totally shadowing the sail segment downstream from any flow particles. However, the current shadowing analysis does not take this into account due to computational requirements. The result is as follows: since the back plate has a resulting force component in a direction opposite a force component for the upstream sail segment, the net force is in fact reduced. While there is a component of force in the freestream direction, the angles of the geometry relative to the freestream result in it being lesser in magnitude than the components that cancelled each other due to the inaccurate shadowing. In the DSMC analysis, this shadowing is automatically taken into account, and there is no falsely calculated force on the downstream sail segment cancelling out a component from the upstream segment. For this reason, the DSMC

shows an increasingly higher force magnitude for each case where the shadowing grows more relevant, while the inaccurate shadowing approximation fails to capture this effect. On the other hand, the geometry of the craft has been designed to maintain a zero, or trim, angle of attack when in the presence of aerodynamic torques. For this reason, these inaccuracies are not as detrimental as they could be if the craft did not passively maintain an orientation where the resulting force calculations are the most accurate. Considerations for future development with shadowing are discussed in the Future Work chapter.

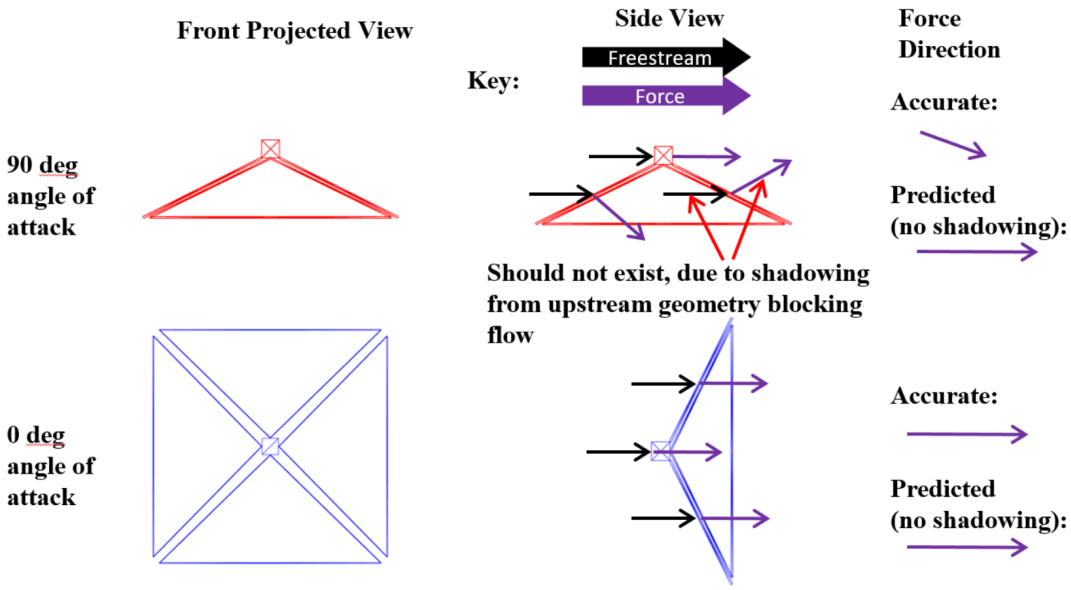

Fig. 5.11. Self shadowing diagram, showing how the simulation falsely identifies certain geometry downstream as "wetted" by the flow

5.4 Conclusions

The ADE case presents an interesting case where the spacecraft orientation stabilizes under the influence of atmospheric torques, but spends the majority of time in orbit well past altitudes where atmospheric effects are noticeable. It was demon-

strated that even with a very loosely bound attitude oscillation at higher altitudes, the geometry of ADE and the inherent offset in the center of pressure and center of mass induce restoring torques that stabilize the spacecraft during perigee passes, working to decrease orbital lifetime - the ultimate goal of the technology that ADE is demonstrating. The self shadowing issue for the ADE geometry was identified using the SPARTA DSMC code. However, it is noted that ADE spends most of its time in the atmosphere closer to a max drag trim orientation than the orientations that showed the most discrepancy between the free molecular and DSMC formulations.

6. CONCLUSION AND FUTURE WORK

6.1 Conclusion

A six degree of freedom simulation tool has been developed for the analysis of coupled orbit attitude motion of spacecraft in Earth orbit. Use of a common STL file format for geometry definition allows for quick comparison in 6DOF behavior for different structures, and modular equations of motion have been used which can allow for the addition of other perturbations in the future. A free molecular aerodynamics formulation has been used along with formulations for solar radiation pressure, gravity gradient torques, and non-spherical gravity potential accelerations to determine deviations from a constant orientation state and two body motion. Three test cases were used with the developed simulation: one validation case involving a spacecraft that has already flown, Lightsail 1, and two predictive test cases for spacecraft that have not yet flown, the SBR assembly and ADE. The 6DOF simulation was able to accurately predict the orbit lifetime of the Lightsail 1 craft using initial conditions from downlinked telemetry packets and a representative STL geometry. The simulation demonstrated that accounting for gravitational, aerodynamic, and solar radiation pressure based perturbations in the context of rotation and translation can produce an accurate state history that closely matches an actual spacecraft orbital lifetime. The SBR experiment demonstrated that an offset of the center of pressure and center of mass can lead to stabilizing effects for a spacecraft in LEO, but only when the atmospheric effects dominate over the gravitational and solar radiation pressure perturbations. The ADE simulation demonstrated that even though the spacecraft may oscillate at a wide range of attitudes for most of a highly elliptical orbit, the stabilizing pyramid sail geometry oriented the spacecraft near the maximum drag orientation during atmospheric passes. The free molecular theory used was shown

to have good agreement with high fidelity DSMC runs in cases where self shadowing is not significant, and discrepancies between the simulation prediction and DSMC prediction were identified at orientations where the effects of shadowing and convex geometries become significant.

6.2 Future Work

There are several aspects that can be improved with regards to the current state of the simulation. First, the code is currently written in MATLAB, which although is a user friendly system for debugging and analysis, is not as fast as languages like C that can be compiled to run optimally on a specific machine, especially for processes like numerical integration. Translating the code to a faster language could open up many possibilities in increasing simulation fidelity without sacrificing significantly more computational time. One example would be the incorporation of a high fidelity shadowing model. Currently, low resolution STL files are used to resolve aerodynamic and solar radiation pressure based surface interactions with good accuracy. Incorporating shadowing could mean requiring higher resolution meshes. Not only would this cause the SRP and aerodynamic calculations to take more time, but the shadowing algorithm itself would take significant time to identify what surface elements are upstream of the flow and to what degree that flow is being blocked. There exist methods for analyzing shadowing using averaged parameters, but this approach would have to be carefully examined to determine applicability with a simulation that is focused on allowing for interchangeable geometry. Another option for this is to allow the user to define the geometry using simple geometric elements like cones, prisms, pyramids, etc., as demonstrated by Hart [43]. This would replace requiring the user to input an STL file, and could draw from pre-determined quantities of aerodynamics and other perturbations to resolve motion. Further, mass distributions can be calculated through the geometry itself if the user defines mass properties to the volume elements, a capability that does not exist with STL files.

Another interesting aspect that has not been addressed in this work is the effect of structural deformation on the motion. In the presence of aerodynamic loads and atmospheric heating, thin membrane sails and tape-spring-like booms could very likely undergo deformations that change the geometry of the spacecraft. This change in geometry would alter the stability characteristics and in turn trajectory of a spacecraft in orbit. Furthermore, surface heating and cooling of a spacecraft can significantly modify the way in which surface particle impingement results in momentum transfer. The analyses of aeroelasticity and transient surface thermal profiles could add a new layer of depth and fidelity to the simulation, and increase the accuracy of its predictive capability.

In the future, it may also be beneficial to incorporate some attitude control capability to the simulation. It could be of interest for the simulation to tell the user what amount of control is necessary to offset the torque loads the simulation calculates at different points in an orbit. Additionally, the ability to add maneuvers to a simulation could also provide more insight on realistic mission scenarios.

A potential point of future analysis is the effect that the spacecraft roll has on stabilization. It was seen that the ADE spacecraft has some constant roll during the simulation time, which may end up spin stabilizing the spacecraft. When the spacecraft enters the atmosphere, this stabilization may be detrimental to re-orienting to the maximum drag orientation, since the stabilizing effect must be temporarily overcome. Finding geometries which may damp this roll could allow the spacecraft to more readily trim to the maximum drag orientation during perigee passes, giving a faster deorbit time.

Finally, more test cases should be run on uncontrolled high area to mass ratio orbiting objects or spacecraft that have both already flown, and also have had their state history recorded. These test cases can provide valuable insight into the strengths and weaknesses of the simulation's predictive ability, and can be used to identify where higher fidelity models are warranted.

REFERENCES

REFERENCES

[1] C. Früh, K. T., and M. Jah, "Coupled orbit-attitude dynamics of high area-to-mass ratio (HAMR) objects: Influence of solar radiation pressure, Earth's shadow and the visibility in light curves," *Celestial Mechanics and Dynamical Astronomy*, vol. 117(4), pp. 385–404, 2013.

[2] T. Schildknecht, R. Musci, M. Ploner, W. Flury, J. Kuusela, J. de Leon Cruz, and L. de Fatima Dominguez Palmero, "An optical search for small-size debris in GEO and GTO," in *Proceedings of the AMOS Technical Conference*, 2003, pp. 1–11.

[3] T. Schildknecht, R. Musci, M. Ploner, G. Beutler, W. Flury, J. Kuusela, J. de Leon Cruz, and L. de Fatima Dominguez Palmero, "Optical observations of space debris in GEO and in highly-eccentric orbits," *Advances in Space Research*, vol. 34, no. 5, pp. 901–911, 2004.

[4] T. Schildknecht, R. Musci, and T. Flohrer, "Properties of the high area-to-mass ratio space debris population at high altitudes," *Advances in Space Research*, vol. 41, no. 7, pp. 1039–1045, 2008.

[5] J. Brodkin, "FCC tells SpaceX it can deploy up to 11,943 broadband satellites," https://arstechnica.com/information-technology/2018/11/spacex-gets-fcc-approval-for-7500-more-broadband-satellites/, accessed: 2019-02-20.

[6] P. B. de Selding, "Boeing proposes big satellite constellations in V- and C-bands," https://spacenews.com/boeing-proposes-big-satellite-constellations-in-v-and-c-bands/, accessed: 2019-02-20.

[7] C. Henry, "OneWeb asks FCC to authorize 1,200 more satellites," https://spacenews.com/oneweb-asks-fcc-to-authorize-1200-more-satellites/, accessed: 2019-02-20.

[8] F. Khan, "Mobile Internet from the Heavens," 2015.

[9] D. J. Kessler and B. G. Cour-Palais, "Collision Frequency of Artificial Satellites: the Creation of a Debris Belt," *J Geophys Res*, vol. 83, no. 6, pp. 2637–2646, 1978.

[10] D. Kessler, N. Johnson, J.-C. Liou, and M. Matney, "The Kessler Syndrome: Implications to future space operations," *Advances in the Astronautical Sciences*, vol. 137, pp. 47–61, 2010.

[11] J. Andringa and D. Hastings, "A systems study on how to dispose of fleets of small satellites," in *AIAA Space 2001 Conference and Exposition*, 2001.

[12] P. C. E Roberts and P. G. Harkness, "Drag Sail for End-of-Life Disposal from Low Earth Orbit," *Journal of Spacecraft and Rockets*, vol. 44, no. 6, 2007.

[13] A. Long and D. Spencer, "Stability of a deployable drag device for small satellite deorbit," in *AIAA/AAS Astrodynamics Specialist Conference, 2016*. American Institute of Aeronautics and Astronautics Inc, AIAA, 2016.

[14] G. Sincarsin and P. Hughes, "Gravitational orbit-attitude coupling for very large spacecraft," *Celestial mechanics*, vol. 31, no. 2, pp. 143–161, 1983.

[15] S. Xu and Y. Wang, "Gravitational orbit-rotation coupling of a rigid satellite around a spheroid planet," *Journal of Aerospace Engineering*, vol. 27, no. 1, pp. 140–150, 2014.

[16] L. Jiang, Y. Wang, and S. Xu, "Integrated 6-DOF Orbit-Attitude Dynamical Modeling and Control Using Geometric Mechanics," *International Journal of Aerospace Engineering*, 2017.

[17] C. Früh, T. Kelecy, and M. Jah, "Attitude dynamics simulation of MLI space debris objects in geosynchronous earth orbits," in *AIAA/AAS Astrodynamics Specialist Conference*, 2012.

[18] C. Früh and M. K. Jah, "Coupled orbitattitude motion of high area-to-mass ratio (HAMR) objects including efficient self-shadowing," *Acta Astronautica*, vol. 95, no. 1, pp. 227–241, 2014.

[19] Q. Li, B. Wang, Z. Deng, H. Ouyang, and Y. Wei, "A simple orbit-attitude coupled modelling method for large solar power satellites," *Acta Astronautica*, vol. 145, pp. 83–92, 2018.

[20] D. Guzzetti, "Coupled orbit-attitude mission design in the circular restricted three-body problem," 2016, dissertation.

[21] V. Tarantini, "Attitude Dependent De-orbit Lifetime Analysis of an Aerodynamic Drag Sail Demonstration Spacecraft and Detailed Thermal Subsystem Design for a Polar Orbiting Communications Nanosatellite," thesis.

[22] A. C. Long, "Development of a Passively Stable Pyramid Sail to Deorbit Small Satellites," dissertation.

[23] J. S. Robinson, "An Overview of NASA's Integrated Design and Engineering Analysis (IDEA) Environment," 2011.

[24] B. Wie, *Space vehicle dynamics and control*, 2nd ed., ser. AIAA education series. Reston, VA: American Institute of Aeronautics and Astronautics, 2008.

[25] L. Roscoe *et al.*, "Stereolithography interface specification," *America-3D Systems Inc*, 1988.

[26] C. W. Hull, "Apparatus for production of three-dimensional objects by stereolithography," Mar. 11 1986, US Patent 4,575,330.

[27] R. H. Battin, *An introduction to the mathematics and methods of astrodynamics*, rev. ed., ser. AIAA education series. Reston, VA: American Institute of Aeronautics and Astronautics, 1999.

[28] P. H. Cowell and A. C. De la Cherois Crommelin, *Investigation of the Motion of Halley's Comet from 1759 to 1910*. Neill & Company, limited, 1910.

[29] D. Brouwer and G. M. Clemence, *Methods of Celestial Mechanics*. Academic Press, 1961.

[30] L. Euler, "Formulae generales pro translatione quacunque corporum rigidorum," *Novi Commentarii academiae scientiarum Petropolitanae*, pp. 189–207, 1776.

[31] W. R. Hamilton, "XI. On quaternions; or on a new system of imaginaries in algebra," *The London, Edinburgh, and Dublin Philosophical Magazine and Journal of Science*, vol. 33, no. 219, pp. 58–60, 1848.

[32] W. B. Chubb, H. F. Kennel, C. Rupp, and S. M. Seltzer, "Flight Performance of Skylab Attitude and Pointing Control System," *Journal of Spacecraft and Rockets*, vol. 12, no. 4, 1975.

[33] A. C. Robinson, "On the use of Quaternions in Simulation of Rigid-Body Motion," Aerospace Research Labs Wright-Patterson Afb OH, 1958.

[34] C. F. Harding, "Solution to Eulers Gyrodynamics I," *Journal of Applied Mechanics*, vol. 31, no. 2, 1964.

[35] R. Mortensen, "Comment on Solution to Eulers gyrodynamics 1," *Journal of Applied Mechanics, Transactions ASME*, vol. 32, no. 1, pp. 228–230, 1964.

[36] B. Wie, H. Weiss, and A. Arapostathis, "Quaternion feedback regulator for spacecraft eigenaxis rotations." *Journal of Guidance, Control and Dynamics*, vol. 12, no. 3, pp. 375–380, 1989.

[37] H.-S. Tsien, "Superaerodynamics, Mechanics of Rarefied Gases," *Journal of the Aeronautical Sciences*, vol. 13, no. 12, pp. 653–664, 1946.

[38] T. I. Gombosi, *Gaskinetic theory*, ser. Cambridge atmospheric and space science series. Cambridge University Press, 1994.

[39] G. A. Bird, *Molecular gas dynamics and the direct simulation of gas flows*. Oxford University Press, 1995.

[40] G. Bird, "Approach to translational equilibrium in a rigid sphere gas," *Physics of Fluids*, vol. 6, no. 10, pp. 1518–1519, 1963.

[41] S. A. Schaaf and P. L. Chambré, *Flow of Rarefied Gases*. Princeton University Press, 1961.

[42] F. Hurlbut, "Fluid flow and heat transfer at low pressures and temperature. an experimental molecular beam investigation of the scattering of molecules from surfaces," Univ. of Calif., Berkeley, Tech. Rep., 1953.

[43] K. Hart, S. Dutta, K. Simonis, B. Steinfeldt, and R. Braun, "Analytically-derived aerodynamic force and moment coefficients of resident space objects in free-molecular flow," in *AIAA Atmospheric Flight Mechanics Conference*, 2014.

[44] J. K. Owens, "NASA Marshall Engineering Thermosphere Model. 2.0," 2002.

[45] R. J. Suggs, "NASA MSFC Solar Activity Forecast," https://sail.msfc.nasa.gov/, accessed: 3/1/2019.

[46] P. Seidelmann, Ed., *Explanatory supplement to the Astronomical almanac*, rev ed. Mill Valley, Calif.: University Science Books, 1992.

[47] D. A. Vallado, *Fundamentals of Astrodynamics and Applications*, 2nd ed. Microcosm Press ; Kluwer Academic Publishers, 2001.

[48] R. M. L. Baker, *Astrodynamics: Applications and Advanced Topics*. New York: Academic Press, 1967.

[49] A. Einstein, "Ist die Trgheit eines Krpers von seinem Energieinhalt abhngig?" *Annalen der Physik*, vol. 323, no. 13, pp. 639–641, 1905.

[50] K. Lambeck, *Geophysical geodesy : the slow deformations of the earth*, ser. Oxford science publications. Oxford University Press, 1988.

[51] D. King-Hele, *Theory of satellite orbits in an atmosphere*. Butterworths, 1964.

[52] P. R. Escobal, *Methods of orbit determination*. R.E. Krieger Pub. Co., [1965]1976.

[53] L. F. Shampine and M. W. Reichelt, "The MATLAB ODE suite," *SIAM journal on scientific computing*, vol. 18, no. 1, pp. 1–22, 1997.

[54] A. A. Alexeenko and S. F. Gimelshein, "Direct Simulation Monte Carlo," in *Handbook of fluid dynamics*, R. W. Johnson, Ed. Crc Press, 2016, ch. 39.

[55] M. A. Gallis, J. R. Torczynski, S. J. Plimpton, D. J. Rader, and T. Koehler, "Direct simulation Monte Carlo: The quest for speed," in *AIP Conference Proceedings*, vol. 1628, no. 1, 2014, pp. 27–36.

[56] A. G. Klothakis, I. K. Nikolos, T. P. Koehler, M. A. Gallis, and S. J. Plimpton, "Validation simulations of the DSMC code SPARTA," in *AIP Conference Proceedings*, vol. 1786, no. 1. AIP Publishing LLC, 2016.

[57] "SPARTA Direct Simulation Monte Carlo (DSMC) Simulator," https://sparta.sandia.gov/index.html, accessed: 2/14/2019.

[58] M. Schoenenberger, A. Dyakonov, and J. V. Norman, "Mars Science Laboratory Aerodynamic Database," NASA Langley Research Center, 2012.

[59] R. W. Ridenoure, R. Munakata, S. D. Wong, A. Diaz, D. A. Spencer, D. A. Stetson, B. Betts, B. A. Plante, J. D. Foley, and J. M. Bellardo, "Testing the lightsail program: Advancing solar sailing technology using a cubesat platform," *Journal of Small Satellites*, vol. 5, no. 2, pp. 531–550, 2016.

APPENDIX

A. 6DOF SIMULATION USER'S GUIDE

The 6DOF simulation developed for and described in this work is a coupled orbit attitude propagator capable of analyzing the rotational and translational motion of spacecraft in elliptical Earth orbits. The code is written in MATLAB, and has been developed for version 2018b. There is one main script in which the run parameters and initial conditions are defined and supplied to the relevant functions. The breakdown of the function calling structure is shown in A.1.

A.1 Summary

There are two modes in which the simulation can operate. The first is a simplified 3DOF "windtunnel" mode, and the second is a full orbital 6DOF mode. The windtunnel only simulates attitude dynamics in the presense of aerodynamic torques, and does not simulate orbital motion. The 6DOF mode simulates coupled orbit attitude motion of a spacecraft, and takes into account aerodynamics, solar radiation pressure, gravity gradient torques, and J_2 perturbations. Both cases require an input of initial orbital and rotational states. The windtunnel simulation uses the initial orbital state to determine the atmospheric properties that will be used for the aerodynamic analysis, whereas the 6DOF mode will use it as an initial condition from which to propagate. Both cases simulate attitude dynamics based on the perturbing torques and initial conditions. While a windtunnel mode run will always run until the time specified by the user, an orbital mode may complete propagation early if the program detects that the spacecraft has dipped below 150km in altitude, signaling a deorbit. Upon completion of the propagation, the simulation will output plots that display all calculated forces and torques, as well as overall attitude state history. For the

6DOF propagation, a figure displaying the 3D orbit geometry and a figure showing the altitude history will also be produced.

Table A.1.
6DOF Simulation function call breakdown

Identifier	**File**	**Functions Called**
1	SixDOF_Main.m	2,4,15
2	Propagation.m	3,5,6,7,8,9,10,13,14,16,17
3	PlotResults.m	5,6,7,8,9,13,16,17
4	MeshData.m	-
5	Perturbations_Aerodynamics.m	-
6	Perturbations_Gravitational.m	-
7	Perturbations_SolarRadiationPressure.m	-
8	AtmosphericProperties.m	11
9	EarthShadow.m	-
10	SunPosition.m	-
11	AirDenTemp.m	12
12	MET.m	-
13	Convert_BODY2NTW.m	-
14	Convert_COES2ECI.m	-
15	Convert_EA2EP.m	-
16	Convert_EP2EA.m	-
17	Convert_NTW2ECI.m	-

A.2 How to Run a Simulation

Running a simulation requires tailoring the input script, $SixDOF\_Main.m$ to be specific to the case being analyzed. The steps to setting up a simulation are as follows.

A.2.1 Defining File Paths

The first section of the $SixDOF\_Main.m$ script defines where the supporting files, geometry files, and supporting functions for the simulation are held. Further, the output directory for all plots generated is also defined. These file paths are defined based on the path of the present working directory, and in most cases do not need to be redefined. If the used desires to store the supporting material elsewhere, these paths must then be redefined. Additionally, if the user wishes to change the directory for the plot outputs, this should be done here.

A.2.2 Defining Geometry

The next section in the $SixDOF\_Main.m$ script is concerned with inputting geometry parameters. The User should enter the file name of the STL geometry they plan to use for the simulation. Note that it is useful to simplify the geometry to reduce the number of triangles on the surface to reduce computational burden. The user must make sure that the STL file being used is in either the same folder that the $SixDOF\_Main.m$ script is in, or in one of the folders that the user specified earlier to add to the path in the previous section (e.g. the 'Geometry Files' folder). The user then has the option of turning on visualization options for the geometry. The first option causes the program to output a figure of the STL file as the program interprets it. The second and third options will turn on or off the the normal vectors and centroid labels for the figure. The final option allows for the user to scale the geometry into the proper dimension of meters. Sometimes, a program will output an

STL file in terms of units like mm or cm. If that is the case, the scale factor adjusts the file data to the correct units. If the STL file is in mm, the user may input 1000 to correct that, if in cm, 100, and so on. It is important to note that CAD software can sometimes erroneously define surface normal vectors for STL geometries while still showing the vertex definitions correctly. The user should be careful to verify normal vector positions using the built in visualization features for each geometry.

A.2.3 Defining Spacecraft Properties

This section is concerned with the other physical properties of the spacecraft besides geometry. First, the user can define a surface temperature for the spacecraft in Kelvin, which effects how the free molecular analytical equations determine the aerodynamic forces and torques. There is currently no capability for the calculation of aerodynamic or radiative heating for the spacecraft, so this value is set and fixed as a constant throughout the run. The next parameter is a surface reflectance coefficient that is used to determine the magnitude at which solar radiation pressure effects the craft. This should be selected based on the materials that the spacecraft is comprised of, and must range from zero to two. A coefficient of zero corresponds to a totally transparent medium, a coefficient of one represents a totally absorbing black body, and a coefficient of two represents a totally reflective surface. The user should next enter the mass of the spacecraft in kg and the inertia matrix of the spacecraft in kgm^2. For the inertia matrix, the user should use the principal moments of inertia, since that is what the equations of motion have been simplified to do. To do this, the spacecraft body axes must be centered with the body center of mass. The next parameter is a vector that can be used to correct for the spacecraft center of mass location. If the origin of the STL file does not coincide with the spacecraft center of mass, this value can be adjusted to align the two points. This vector should be expressed in meters regardless of the units of the STL file, since the scale factor used in the previous section will work to adjust the geometry into meters.

A.2.4 Miscellaneous Settings

Here, the user may specify whether the windtunnel analysis or obrital 6DOF analysis is used by the program. The windtunnel mode can give insight on attitude behavior of an object in a free molecular flow regime, and the 6DOF simulation should be used when understanding of the spacecraft trajectory and orientation in an orbital context is required. Additionally, the user can custom define the solver tolerances used during numerical integration of the equations of motion.

A.2.5 Defining Time Settings

The user should first input an epoch in the format dd-mm-yyyy HH:MM:SS in this section. This epoch is used to both calculate the sun position vector for SRP and Earth shadow calculations, and to determine solar cycle activity so as to more accurately model the atmosphere. Note that there is by default a file in the supporting functions directory along the lines of 'MSFC Solar Flux Data' which holds the data needed by the atmospheric properties determination functions to properly model the atmosphere. This file is valid for a specific range of epochs based on the information published by Marshall Space Flight Center on the solar activity forecast page at https://sail.msfc.nasa.gov/. The user may get an error if the epoch they are attempting to use lies outside of the epochs defined by this file. If so, the user should visit the government site to acquire the data needed. If the epoch is too far in the past or future, data may not be available, and the user may need to manually input data into the file for a specific date. Next, the user should input the time for propagation. In windtunnel mode, the propagation will always carry out to the final time specified by the user. In orbital 6DOF mode, there is a chance that the simulation may detect that the spacecraft has deorbited if the altitude goes below 150 km. If the spacecraft has deorbited, the simulation will end and data will be available for all timesteps leading up to deorbit. The user may sometimes wish to use the software to predict deorbit, in which a large propagation time should be used, so the simulation

may determine when the deorbit occurs. Should the user wish to change the value at which the simulation determines deorbit has occurred, the check value in the *Deorbit* subfunction of *Propagation.m* should be altered.

A.2.6 Defining Initial State

In this section, the user can enter the initial translational and rotational state of the spacecraft. The program is designed for the user to input the initial orbital state in classical Keplerian orbital elements. The semi-major axis length should be given in km, while the initial inclination, argument of perigee, right ascension of the ascending node, and true anomaly should all be given in radians. In the sample orbits provided, there is a build in conversion from degrees to radians using the matlab $deg2rad$ function, so the user should be mindful not to double convert. The eccentricity is dimensionless, and should be entered as a value less than one. The simulation currently does not support parabolic or hyperbolic orbit geometries. Further, the only central body currently supported is the Earth.

After entering the orbital elements, the user can specify an initial orientation in terms of roll, pitch and yaw. The sequence used for rotations is a body 1-2-3, meaning roll would be about the x axis, pit would be about the y axis, and yaw would be about the z axis. The x axis of the craft should nominally point in the direction of the spacecraft velocity unless perturbed, the user is encouraged to use the built in geometry viewing capabilities of the software described in the first section to make sure that the axes are properly defined in the way the software expects them. The user may finally decide to apply intial angular rates about the three axes to the spacecraft as well. All initial angles and angular rates should be entered in degree and degrees per second, respectively. The software later converts the orbital state to position and velocity vectors in the Earth Centered Inertial frame, and the orientation is converted to a quaternion representation for propagation.

The program is ready to run after setting the initial 6DOF state in this section.

A.3 Simulation Logic

This section outlines the logical path the simulation takes, and can be used to help give the user an idea of the thought process behind the code.

A.3.1 Mesh Generation

The first step of the simulation after running the $SixDOF\_Main.m$ script, regardless of if windtunnel mode or 6DOF mode was selected, is to read the STL file and generate the mesh data. The STL file is provided to $MeshData.m$, which determines if the STL file is in ASCII or binary format, and then reads the vertex and face data to create a triangular mesh. Using the vertex data, $MeshData.m$ find the centroid of each triangle, as well as the area of each triangle. If the user specified for the geometry to be displayed, $MeshData.m$ will display the geometry. $MeshData.m$ returns the surface element areas, centroids, and normal vectors to the $SixDOF\_Main.m$ script.

A.3.2 Propagation

The $SixDOF\_Main.m$ script next sends the initial conditions defined by the user as well as the geometry information calculated by $MeshData.m$ to the $Propagation.m$ function. The remainder of the simulation will occur within this function. The first step in $Propagation.m$ is to parse the user defined run parameters into a set of initial conditions depending on if windtunnel or 6DOF mode was selected. To do this, the function converts the classical orbital elements into an r and v vector set using the $Convert\_COES2ECI.m$ function, and then compiles the initial conditions into one vector variable. The function then proceeds based on if the user specified 6DOF (orbital) or 3DOF (windtunnel) mode using a conditional selection.

A.3.3 6DOF Mode

6DOF mode begins in the *Propagation.m* function after the initial conditions are parsed if the user did not select windtunnel mode in the *SixDOF_Main.m* script. First, the ODE solver options are set based on what the user set as the integration tolerances, and since this is 6DOF mode, an event for detecting deorbit (default: if altitude ¡ 150km) is also set as part of the options. Next, the sun position vector is determined for use in calculating the solar radiation pressure and shadowing. Currently, the sun position is not updated from where it is located at the initial epoch. For short integration times, this is valid, but can lead to inaccuracies when considering very long propagation times. The *Propagation.m* function then hands off control to the ode113 function, which solves the system of differential equations in the *Propagation.m* subfunction, *Orbitalcase*. Here, the initial state vector is parsed. First, the initial quaternions and angular rates are obtained, and then an Euler angle representation of the orientation state is obtained by using the conversion function *Convert_EP2EA.m*. Further, a relation between the NTW frame and the body axis reference frame is obtained using *Convert_BODY2NTW.m*. The translational state is then parsed into the relevant r and v vectors, and a relation between the NTW and ECI frames is obtained using the *Convert_NTW2ECI.m*. With the current state and relevant frame rotations obtained, the subfunction then determines the atmospheric properties based on the current state and epoch using the Marshall Engineering Thermosphere model codes using *AtmopshericProperties.m*, *AirDenTemp.m*, and *MET.m*. After determining the freestream conditions, the Earth shadow state is obtained using *EarthShadow.m*. This function determines whether the spacecraft is in Earth's umbra, penumbra, or neither.

Upon determining these environmental parameters, the perturbations can then be calculated from aerodynamic, SRP, and gravitational sources. Each group of perturbations has a corresponding torque and force that perturb the orientation and trajectory, respectively.

Aerodynamic Perturbations

The *Perturbations_Aerodynamics.m* function calculates all aerodynamic perturbations. The function receives freestream properties, spacecraft geometry and parameters, and rotation matrices from *Propagation.m*. The function cycles through every surface element and uses the subfunction FMFC to determine the pressure and shear coefficients on the surface element using free molecular analytical equations. The function uses the forces and centroids to determine torques for each element, and then sums the forces and torques to get the net body torque and force. The acceleration is then found using the spacecraft force and mass. These values are converted to the proper reference frames for propagation and then returned to the *Propagation.m* function. Note that this function contains the definitions of the accommodation coefficients. If the user desires to modify them from the current approximation (totally diffuse collisions), that can be done in this function.

Solar Radiation Pressure Perturbations

The *Perturbations_SolarRadiationPressure.m* fucntion is used to calculate perturbations from SRP. *Propagation.m* passes information on the reflectivity coefficient , spacecraft position, Earth shadow state, spacecraft geometry properties, and the rotation matrices to the function. Similar to how the aerodynamics function calculates the forces on every surface element, the *Perturbations_SolarRadiationPressure.m* function cycles through every element and determines force and torque, and subsequently sums to find the net effects. If the spacecraft is in Earth's umbra, these values are not calculated and instead set to zero. In penumbra, the values are calculated and halved. The acceleration is again found by using the force and spacecraft mass. The acceleration and torque values are returned to the *Propagation.m* function after the relevant frame conversions.

Gravitational Perturbations

The *Perturbations_Gravitational.m* function is called by the *Propagation.m* function to find the gravity gradient torque and J2 perturbing effect on trajectory. The function takes the current position vector, Earth properties, spacecraft properties, and frame conversions from the *Propagation.m* function. This function does not need to operate on the individual surface elements to determine forces and torques unlike the other perturbation functions. Here, the J2 acceleration is determined using a simple analytical model, and the gravity gradient torque is determined based on the spacecraft orientation and inertia properties. Conversions are mostly used here to put the input values in the proper frames for calculation. Acceleration and torque terms are then returned to the *Propagation.m* function.

Equation of motion integration

When all of the perturbing effects have been accounted for, the accelerations can be summed and used to perturb the two body motion using Cowell's formula, and the torques can be applied to the dynamic equations of motion to determine the resulting angular rates, from which the orientation is determined using the kinematic equations of motion. The integration is performed on a variable time step to satisfy the user specified integration tolerance, and the attitude and trajectory are calculated simultaneously. Upon successful integration, the state vector is returned from *Orbitalcase* to *Propagation.m*, and the ode function then integrates the next timestep, recalculating all torques, forces and accelerations. This continues until either the final time arrives, or the simulation breaks the propagation after detecting an orbit altitude below 150 km. When this happens, the propagation is complete and the state data is passed to the *PlotResults.m* function.

Plotting results

The *PlotResults.m* function takes all of the data from the simulation and compiles them into a series of plots for user visualization, and then saves them to the directory specified by the user. First, the program checks if the directory specified by the user exists, and if not, it is created. Next, the function recalculates the perturbation values found for every timestep in the propagation. This is done because the variable timestep integrator used for integration does not have the capability of storing intermediate information such as the forces and torques, only the end result, the spacecraft state, is integrated. This cannot be mitigated by using persistent or global variables since the integrator frequently backtracks timesteps when integration tolerances are not met, so if in actuality there is one timestep between state A and state B in a simulation, saving the values persistently may provide four extra data sets, which do not reflect the actual values used to integrate the motion. A more elegant solution may exist, but this brute force method is sufficient and reduces the amount of error by directly calculating the perturbations from the state history. When recalculation is finished, the plots will be displayed to the user, and the command window will tell the user where they have been saved.

A.3.4 3DOF Mode

In 3DOF mode, the simulation determines the freestream parameters outside of the main integration loop, since the position will not be updated, and the freestream should thus be persistent among all timesteps. Using this persistent freestream, the *Propagation.m* function solves for the orientation state in the *Windtunnelcase* subfunction using MATLAB's built in ODE solvers. Like in the 6DOF case, the data is first parsed, and then the body to NTW frame conversion occurs. In this case however, only the aerodynamic torque is calculated using the *Perturbations_Aerodynamic.m* function, with no other perturbations considered. The dynamic equations of motion are solved using this torque for the angular rates, and then the kinematic equations of

motion are solved to give the orientation state in terms of quaternions. Unlike in the 6DOF simulation, this integration will always carry out to the final time specified by the user. Upon completion, the *PlotResults.m* function will be called. Here, only the aerodynamics will be calculated, and there will be no orbit or altitude plots supplied.

A.4 How to Add Perturbations

Since the equations of motion can account for additional perturbations through linear summations, adding additional sources of perturbations is simple. The user will need to create a function that can output the accelerations, torques, and forces due to the perturbation, and then sum the results in the subfunction *Orbitalcase* of the *Propagation.m* function. Further, the user should add the function in the recalculation section of the *PlotResults.m* function. If the perturbation requires more input variables than the *Propagation.m* function can currently provide, there should be sections added in the *SixDOF_Main.m* script so that variables can readily be changed between runs. For a general reference that includes many types of perturbation sources, the user is directed to Vallado [47].

B. SPARTA DSMC RUN PARAMETERS

The SPARTA DSMC software was used as a comparison to the free molecular methods used in the 6DOF simulation. SPARTA operates off of a user provided input script that directs the software to perform specific actions and use specific flow parameters. For each SPARTA case ran, the freestream data was obtained from the 6DOF simulation, such that the simulated flow would be identical between each SPARTA and 6DOF comparison case. The differences in results could then be attributed to the way each system solved for the forces on the geometries. All geometries used were constant between the types of cases as well. In short, given one geometry and one set of freestream conditions, a result for force magnitude was obtained using both the 6DOF and SPARTA formulations. Table B.1 shows the more detailed parameters behind each DSMC run.

Table B.1.
SPARTA DSMC Parameters

Case	**# den**	**Domain [m]**	**Grid**	**fnum**	**Step [s]**	**Seed**
Lightsail	1.600e14	6x6x6	100x100x100	1.728e9	8e-6	12345
SBR	1.849e12	36x36x36	100x100x100	4.431e9	5e-5	12345
ADE	1.337e16	2x2x2	100x100x100	6.687e8	2e-7	12345

The ratio of real to simulated particles, fnum, was calculated by requiring that at least 20 simulated particles should occupy the smallest volume element defined by the grid, which was done by accounting for the domain size, grid size, and number density. The time step was calculated by requiring that at least five time steps are required for a particle to pass from one end of a grid cell to the other. Domain sizing

was done by rounding up the maximum dimension of the craft. There was no concern for cutting the flowfield off to soon with this approach since no diffuse shocks are expected, due to the extremely rarefied nature of the flows (no flows here have a Knudsen number below 100).

For each case, the variable soft sphere collision model was used. For the species composition and ambient temperature, the Marshall Engineering Thermopshere model was used, just as in the 6DOF simulation. All flow parameters were found at the closest approach for each case. This means perigee for Lightsail and ADE, since they have elliptical orbits, and at a 650 km circular orbit for the SBR system. For all cases, a nonracting flow was assumed, and the simulations were run using 20 cores for four hours on a supercomputer cluster.